

Impaired ketogenesis ties metabolism to T cell dysfunction in COVID-19

<https://doi.org/10.1038/s41586-022-05128-8>

Received: 28 July 2021

Accepted: 20 July 2022

Published online: 28 July 2022

 Check for updates

Fotios Karagiannis^{1,15}, Konrad Peukert^{2,15}, Laura Surace^{1,2,15}, Marcel Michla¹, Fabian Nikolka³, Mario Fox², Patricia Weiss¹, Caroline Feuerborn², Paul Maier¹, Susanne Schulz², Burcu Al⁴, Benjamin Seeliger⁵, Tobias Welte⁵, Sascha David⁶, Inge Grondman⁷, Aline H. de Nooijer⁷, Peter Pickkers⁸, Jan Lukas Kleiner², Marc Moritz Berger⁹, Thorsten Brenner⁹, Christian Putensen², Bonn COVIMMUNE Consortium*, Hiroki Kato¹⁰, Natalio Garbi¹¹, Mihai G. Netea^{4,7}, Karsten Hiller³, Katarzyna Placek^{4,16}, Christian Bode^{2,16}✉ & Christoph Wilhelm^{1,16}✉

Anorexia and fasting are host adaptations to acute infection, and induce a metabolic switch towards ketogenesis and the production of ketone bodies, including β -hydroxybutyrate (BHB)^{1–6}. However, whether ketogenesis metabolically influences the immune response in pulmonary infections remains unclear. Here we show that the production of BHB is impaired in individuals with SARS-CoV-2-induced acute respiratory distress syndrome (ARDS) but not in those with influenza-induced ARDS. We found that BHB promotes both the survival of and the production of interferon- γ by CD4⁺ T cells. Applying a metabolic-tracing analysis, we established that BHB provides an alternative carbon source to fuel oxidative phosphorylation (OXPHOS) and the production of bioenergetic amino acids and glutathione, which is important for maintaining the redox balance. T cells from patients with SARS-CoV-2-induced ARDS were exhausted and skewed towards glycolysis, but could be metabolically reprogrammed by BHB to perform OXPHOS, thereby increasing their functionality. Finally, we show in mice that a ketogenic diet and the delivery of BHB as a ketone ester drink restores CD4⁺ T cell metabolism and function in severe respiratory infections, ultimately reducing the mortality of mice infected with SARS-CoV-2. Altogether, our data reveal that BHB is an alternative source of carbon that promotes T cell responses in pulmonary viral infections, and highlight impaired ketogenesis as a potential confounding factor in severe COVID-19.

Sickness behaviours are an evolutionarily preserved coordinated set of adaptive behavioural changes, including lethargy, fever, social withdrawal and loss of appetite, that have evolved to support the survival of the host in response to infections^{1–3}. Human and animal data show that infection-induced anorexia and the induction of ketogenesis—a well-described host metabolic adaptation in response to fasting⁴—are promoted in the context of respiratory viral infections^{5,6}. This indicates that infectious diseases and host metabolism are intimately linked⁷. However, the physiological role of ketogenesis during an infection remains unclear². Although host metabolic adaptations that are shaped by evolutionary pressure in response to endemic viruses are conserved⁷, they may be dysfunctional in the context of emerging zoonotic infections. This idea is of particular note in light of the current pandemic of COVID-19, which is caused by the zoonotic virus SARS-CoV-2 (refs. ^{8,9}). In the

majority of infected people, the host immune response is sufficient to resolve the infection. In some cases, however, dysfunctional immune responses may result in severe pathology in the lungs and systemically^{10,11}. Two of the main cellular immune populations involved in the clearance of the viral infections are CD4⁺ type 1 helper T (T_H1) cells and CD8⁺ cytotoxic T cells, which act through the production of cytokines such as interferon- γ (IFN γ) and through the killing of infected cells. Cellular metabolism and mitochondrial function are major determinants of T cell activation and function¹², which raises the question of a potential link between infection-induced ketogenesis and T cell immunity.

To investigate a possible connection between infection-induced metabolic alterations and immune responses in the host in the context of severe pulmonary infections, we examined differences in viral-infection-related ketogenesis. This was achieved by assessing

¹Immunopathology Unit, Institute of Clinical Chemistry and Clinical Pharmacology, Medical Faculty, University Hospital Bonn, University of Bonn, Bonn, Germany. ²Department of Anesthesiology and Intensive Care Medicine, University Hospital Bonn, Bonn, Germany. ³Department of Bioinformatics and Biochemistry, Braunschweig Integrated Center of Systems Biology, Technische Universität Braunschweig, Brunswick, Germany. ⁴Immunology and Metabolism Unit, Life & Medical Sciences Institute (LIMES), University of Bonn, Bonn, Germany. ⁵Department of Respiratory Medicine and German Centre of Lung Research (DZL), Hannover Medical School, Hannover, Germany. ⁶Institute of Intensive Care Medicine, University Hospital Zürich, Zürich, Switzerland. ⁷Department of Internal Medicine and Radboud Center for Infectious Diseases, Radboud University Medical Center, Nijmegen, The Netherlands. ⁸Department of Intensive Care Medicine and Radboud Center for Infectious Diseases, Radboud University Medical Center, Nijmegen, The Netherlands. ⁹Department of Anesthesiology and Intensive Care Medicine, University Hospital Essen, University Duisburg-Essen, Essen, Germany. ¹⁰Institute of Cardiovascular Immunology, University Hospital Bonn, University of Bonn, Bonn, Germany. ¹¹Institute of Experimental Immunology, Medical Faculty, University Hospital Bonn, University of Bonn, Bonn, Germany. ¹²These authors contributed equally: Fotios Karagiannis, Konrad Peukert, Laura Surace. ¹⁶These authors jointly supervised this work: Katarzyna Placek, Christian Bode, Christoph Wilhelm. *A list of authors and their affiliations appears at the end of the paper.

✉e-mail: christian.bode@ukbonn.de; christoph.wilhelm@uni-bonn.de

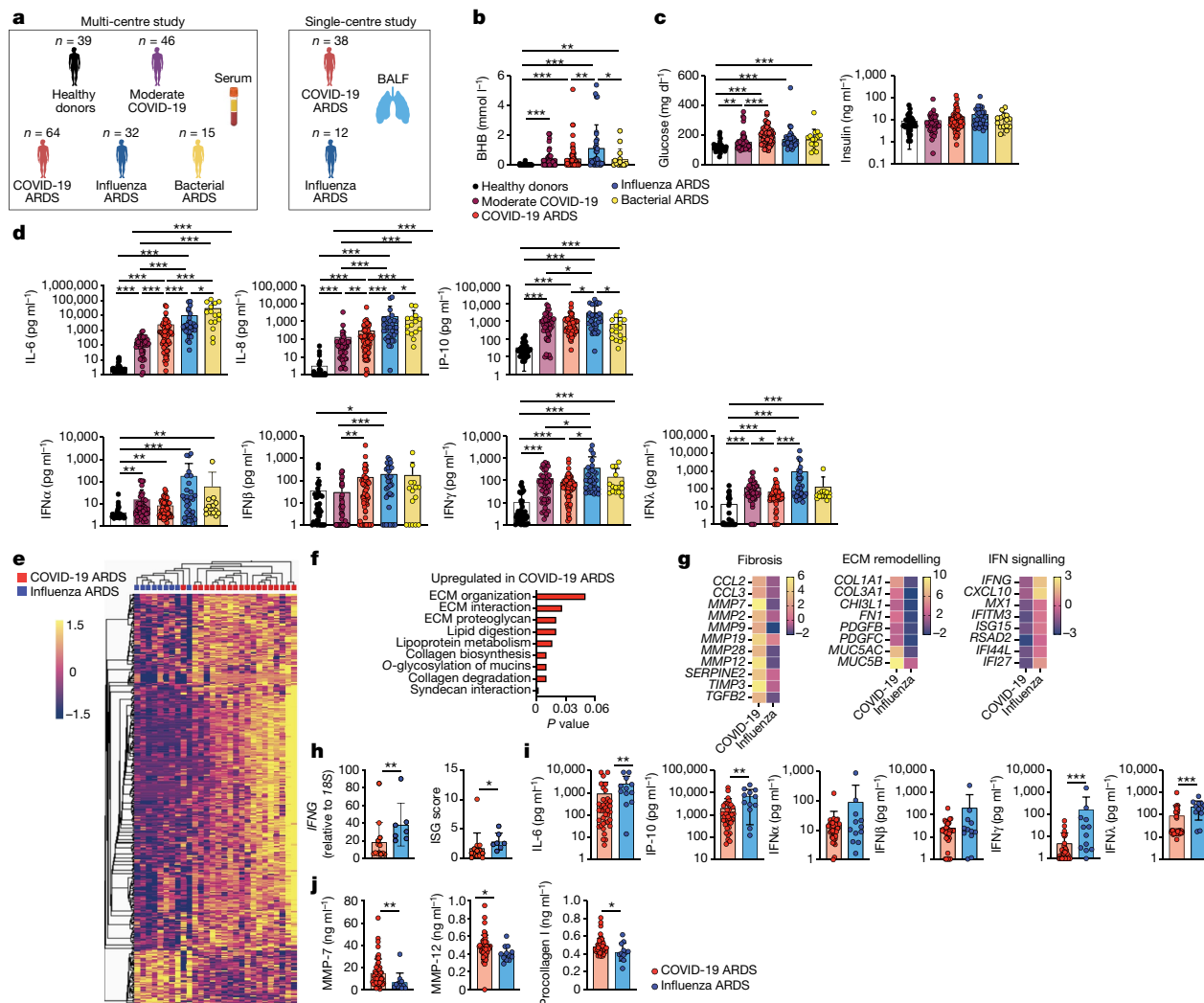


Fig. 1 | Impaired production of BHB and IFN γ in severe COVID-19.

a, Overview of the cohorts and the samples included in the study. Figure created using BioRender.com. **b**, Serum concentration of BHB in healthy donors ($n = 39$; black), patients with moderate COVID-19 ($n = 46$; purple) and patients with ARDS due to COVID-19 ($n = 64$; red), influenza ($n = 32$; blue) or bacterial pneumonia ($n = 15$; yellow). **c, d**, Serum concentration of glucose and insulin in the indicated cohorts (**c**) and quantification of pro-inflammatory cytokines in the serum (**d**). **e–g**, RNA-seq analysis of cells from the BALF from patients with COVID-19 ARDS ($n = 19$; red) and influenza ARDS ($n = 9$; blue). **e**, Heat map of differentially expressed genes ($P < 0.05$) (around 700 differentially expressed genes in total). **f**, Pathway analysis. **g**, Heat maps showing the fold change of genes associated with fibrosis, extracellular matrix

(ECM) remodelling and interferon signalling. **h**, Relative expression of *IFNG* and ISG score (as a mean of interferon-stimulated gene (ISG) expression; *IFITM3*, *IFI27*, *IFI44L*, *IFIT1*, *MX1*, *ISG15*, *MX2*, *RSAD2* and *SIGLEC1*) in the BALF of patients with COVID-19 ARDS ($n = 13$) and influenza ARDS ($n = 7$). **i, j**, Quantification of the indicated cytokines (**i**) and fibrotic biomarkers (**j**) in the BALF of patients with COVID-19 ARDS ($n = 38$) and influenza ARDS ($n = 12$) ARDS. In **b–d, h–j**, each dot represents a donor. Data are mean \pm s.d. Statistics were assessed by non-parametric one-way ANOVA (Kruskal–Wallis test) corrected for multiple comparisons by two-stage linear step-up procedure of Benjamini, Krieger and Yekutieli (**b–d**), or by two-tailed Student’s *t*-test (**h–j**); not significant (not indicated), $P > 0.05$; * $P < 0.05$; ** $P < 0.01$; *** $P < 0.001$.

the production of the ketone body BHB in mice infected with influenza A virus (IAV) (Extended Data Fig. 1), in the peripheral blood of patients with COVID-19 who were hospitalized (termed ‘moderate’), and in the peripheral blood of ventilated patients with ARDS caused by SARS-CoV-2, influenza or bacterial respiratory infections, with the latter included as a non-viral control (Fig. 1a and Extended Data Table 1).

Ketogenesis is impaired in COVID-19

Mice that were infected with IAV showed a reduction in body weight, food consumption and glucose levels, but an increased concentration of BHB in the serum and an upregulation of genes encoding enzymes that control ketogenesis in the liver (*Hmgcs2* and *Cpt1*) (Extended Data Fig. 1a–c). Consistent with the mouse data, levels of BHB were increased

in the serum of patients with influenza in comparison to healthy control individuals, indicative of infection-induced ketogenesis (Fig. 1b). By contrast, patients with moderate and severe COVID-19, but also patients with bacterial pneumonia, had low concentrations of BHB (Fig. 1b). This suggests that infection-induced ketogenesis may be compromised in COVID-19 ARDS. Notably, pre-existing metabolic disorders, including high blood glucose in type 2 diabetes and obesity, are major risk factors for increased lethality in patients with COVID-19 (refs. 13,14). Both insulin and glucose are routinely administered to patients with ARDS, together with enteral and parenteral feeding, to maintain stable concentrations of blood glucose. We observed increased concentrations of glucose in patients with COVID-19 ARDS in comparison to patients with moderate COVID-19 and healthy control individuals (Fig. 1c). However, we did not find a substantial difference in the concentration of

glucose or insulin, or in the total calories supplied, between COVID-19 and influenza or bacterial ARDS (Fig. 1c and Extended Data Fig. 2a,b). Moreover, neither the total amount of supplied calories nor the concentration of blood glucose correlated with systemic levels of BHB (Extended Data Fig. 2c,d), thus arguing against the involvement of these parameters in the differential regulation of BHB production. In line with previous reports^{15–17}, patients with severe COVID-19 had increased concentrations of inflammatory cytokines in comparison to patients with moderate symptoms or uninfected control individuals (Fig. 1d). However, patients who were infected with SARS-CoV-2 showed substantially lower expression of the inflammatory cytokines interleukin (IL)-6 and IL-8, in comparison to patients with influenza- or bacteria-induced ARDS (Fig. 1d). This challenges the initial hypothesis of a cytokine storm, and indicates that immune dysregulation could be a major driver of severe COVID-19, as has been suggested previously^{18,19}. Most notably, we observed lower concentrations of interferon-related cytokines, including IFN γ , IFN λ and IFN γ -induced protein-10 (IP-10), in patients with COVID-19 relative to patients with influenza (Fig. 1d). We did not find any significant difference in type I interferons (Fig. 1d). To validate our findings at the site of infection, we next performed a bulk RNA-sequencing (RNA-seq) analysis of cells from bronchoalveolar lavage fluid (BALF) that was isolated from patients with severe COVID-19 and patients with influenza. Despite the high degree of transcriptional similarity (Extended Data Fig. 3a; Gene Expression Omnibus (GEO) accession code GSE207077), pathway analysis revealed an enrichment in genes related to the remodelling of the extracellular matrix and pulmonary fibrosis in COVID-19 ARDS (Fig. 1e–g). On the other hand, genes associated with interferon signalling were increased in influenza ARDS, which we further confirmed by quantitative PCR with reverse transcription (qRT-PCR) (Fig. 1h and Extended Data Fig. 3b). Supporting our findings in peripheral blood, pro-inflammatory cytokines and factors that mediate antiviral defence were markedly reduced in the BALF of patients with COVID-19 ARDS compared to the influenza cohort (Fig. 1i). We also detected a significant increase in proteins related to pulmonary fibrosis in the BALF of COVID-19 ARDS (Fig. 1j), in agreement with the finding that collagen deposition and the development of fibrosis is particularly pronounced in COVID-19, in contrast to influenza ARDS²⁰.

An impaired CD4⁺ T cell response has been suggested to be a hallmark of severe COVID-19 (refs. ^{21–27}). Previous work reported the beneficial effects of a ketogenic diet during IAV or coronavirus infections in mice^{28,29} or found that BHB promotes the function of effector and memory CD8⁺ T cells^{30,31}. However, it is unclear whether and how ketogenesis influences CD4⁺ T cell immunity. To investigate this aspect, we added BHB to CD4⁺ T cells in diluted cell culture medium (1:1 with phosphate-buffered saline (PBS)), to more closely resemble the limited availability of nutrients in infection. T_H1-polarized human and mouse CD4⁺ T cells showed an increase in numbers and enhanced production of IFN γ but not tumour necrosis factor (TNF) when cultured with BHB (Fig. 2a,b and Extended Data Fig. 4a–h). Consistent with previous reports³¹, BHB had a similar effect on CD8⁺ T cells (Extended Data Fig. 4a–h). Of particular note, knockdown of the gene *BDHI*, which mediates ketolysis (Fig. 2c and Extended Data Fig. 4i,j), reverted the BHB-induced increase in IFN γ in both mouse and human T_H1 cells (Fig. 2d,e). The BHB-mediated expansion of T_H1 cells was not due to accelerated proliferation (Ki-67; Extended Data Fig. 4k–n), but dependent on increased survival (annexin V; Extended Data Fig. 4o). Thus, BHB may be an important fuel to support the fitness of T cells in nutrient-deprived microenvironments in severe virus-induced inflammation.

BHB supports mitochondrial metabolism

In light of the ability of BHB to alter the functionality of CD4⁺ T cells, we used extracellular flux analysis. Addition of BHB increased both the basal and the maximal rate of mitochondrial respiration and enhanced the spare respiratory capacity after short-term (day 3) (Extended Data

Fig. 5a) and long-term (day 6) culture of mouse T_H1 cells (Fig. 2f). This increase in OXPHOS appears to be independent of glucose (Extended Data Fig. 5b,c). Notably, ablation of OXPHOS by simultaneous inhibition of complex I, III and V of the respiratory chain reduced the capacity of human CD4⁺ T cells to produce IFN γ and TNF (Extended Data Fig. 5d,e), without affecting their survival (Extended Data Fig. 5f). We further established the ability of BHB to enhance the mitochondrial functionality of CD4⁺ T cells with SCENITH (single-cell energetic metabolism by profiling translation inhibition)³². Using SCENITH on cultured mouse and human T_H1 CD4⁺ T cells, we confirmed that adding BHB to CD4⁺ T cells increased the mitochondrial dependence and reduced the glycolytic capacity (Extended Data Fig. 5g,h). However, these metabolic adaptations were highly dependent on BDHI-mediated ketolysis (Fig. 2g). Likewise, we observed that BDHI increased the ability of activated CD4⁺ T cells to metabolize fatty acids and amino acids in the presence of BHB while reducing their glucose dependence; this indicates that there is some flexibility in nutrient usage, which is crucial to support cellular fitness (Fig. 2g, Extended Data Fig. 5g,h). Moreover, in line with the role of BHB in supporting OXPHOS in CD8⁺ T cells³¹ we observed similar metabolic changes when human (but not mouse) CD8⁺ T cells were cultured with BHB (Extended Data Fig. 6a–c). As increased OXPHOS and mitochondrial function have been linked to the capacity of cells to produce IFN γ ^{33,34}, BHB-dependent bolstering of OXPHOS may act preferentially to promote the effector function of CD4⁺ T cells.

BHB provides an alternative fuel for T cells

To further investigate the metabolism of BHB in CD4⁺ T cells, we performed tracing of ¹³C-labelled BHB in cultured mouse T_H1 cells. ¹³C-tracing experiments revealed that T_H1 cells can use BHB as a carbon source for intermediates in the tricarboxylic acid (TCA) cycle (Fig. 3a and Supplementary Table 1). By contrast, carbons from ¹³C-labelled glucose were exclusively incorporated into intermediates of glycolysis and the pentose phosphate pathway (Fig. 3a and Supplementary Table 1). Moreover, labelled carbons from BHB were also found in bioenergetic amino acids (glutamate and aspartate) and oxidized glutathione (GSSG) (Fig. 3a), whereas the reduced form (GSH) was not detected (Supplementary Table 1). We confirmed the integration of BHB in TCA cycle intermediates and bioenergetic amino acids in CD4⁺ T cells in IAV-infected mice in vivo and ex vivo (Extended Data Fig. 7a,b). As balanced levels of cellular reactive oxygen species (ROS) are crucial for maintaining T cell function^{12,35}, glutathione oxidation might be a mechanism that is exploited by T cells to avoid ROS-induced oxidative stress caused by enhanced OXPHOS. Indeed, we found no significant increase in cellular ROS after the addition of BHB (Extended Data Fig. 7c). Furthermore, when we examined the expression of genes encoding enzymes that act as metabolic gatekeepers in CD4⁺ T cells, we found a BHD-induced upregulation of *Cpt1* (fatty acid oxidation), *Got1* (amino acid metabolism), *Ndufs8* (OXPHOS), *Sdha*, *Sdhb*, *Sdhc* (TCA cycle) and *Txnrd1* (redox balance) (Fig. 3b and Extended Data Fig. 7d). Notably, severe COVID-19 is characterized by amino acid catabolism and a reduction in the levels of circulating amino acids^{36,37}. We therefore analysed a previously published metabolomic dataset of patients with COVID-19 with different levels of disease severity (1–7, quantified by the World Health Organization ordinal scale)³⁶. Consistent with previous reports, we found reduced amounts of tryptophan, bioenergetic amino acids and cysteine in the serum of patients with COVID-19 ARDS (Fig. 3c), indicating an overall reduction in amino acid availability. Reduced cysteine suggests a possible impairment in the GSH/GSSH balance and the cellular oxidation state (Fig. 3c). We did not observe any change in valine (a branched-chain amino acid) or lysine (Extended Data Fig. 7e), which are crucial for T cell activation and function³⁸. Notably, addition of BHB was able to increase the numbers and functionality of cultured human CD4⁺ T cells, even in the absence of amino acids (Fig. 3d and Extended Data Fig. 7f). Thus, our data show that BHB acts as an alternative carbon source that promotes

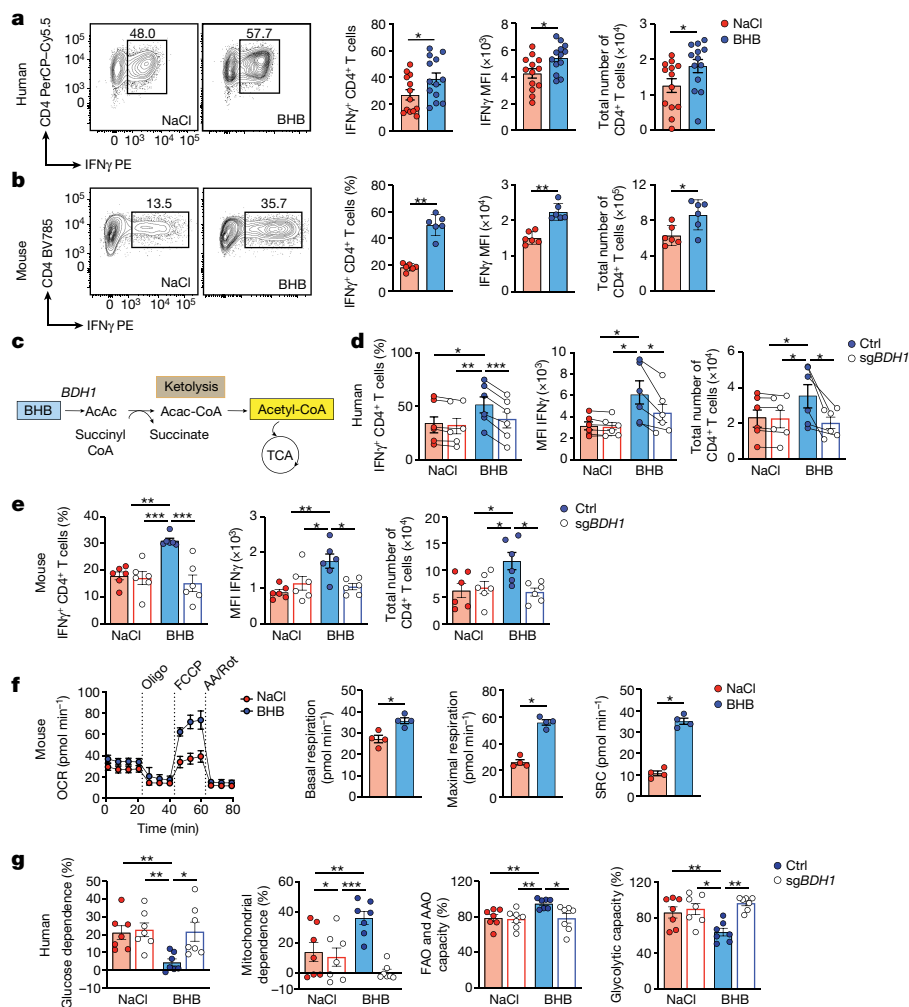


Fig. 2 | BHB promotes the production of IFN γ and OXPHOS in CD4⁺ T cells. **a, b, d–g.** Human CD4⁺ T cells isolated from the blood of healthy donors (**a, d, g**) or splenic mouse CD4⁺ T cells (**b, e, f**) were cultured in T_H1 polarizing conditions in the presence or absence of 5 mM BHB. **a, b,** Representative flow plots and percentage of IFN γ ⁺ CD4⁺ T cells, IFN γ geometric mean fluorescence intensity (gMFI) and total number of live cells (human CD4⁺ T cells, $n = 13$; mouse CD4⁺ T cells, $n = 6$). **c,** Schematic representation of ketolysis. AcAc, acetoacetate; AcAc-CoA, acetoacetyl-CoA. **d–g,** Human CD4⁺ T cells or splenic mouse naive CD4⁺ T cells ($n = 6$) were mock treated or nucleofected with *BDH1*-targeting (*sgBDH1*) sgRNA–Cas9 RNPs and cultured in T_H1 conditions in the presence or absence of 5 mM BHB. **d, e,** Percentage of IFN γ ⁺ CD4⁺ T cells,

IFN γ gMFI and live cell count analysed by flow cytometry ($n = 6$). **f,** Energy metabolism analysed by extracellular flux analysis on day 6 ($n = 4$). Oligo, oligomycin; AA/Rot, antimycin A and rotenone; OCR, oxygen consumption rate; SRC, spare respiratory capacity. **g,** Bioenergetic characterization by SCENITH ($n = 7$). FAO, fatty acid oxidation; AAO, amino acid oxidation. In **a, d, g,** each dot represents a donor. Data in **b, e, f** are representative of three independent experiments with $n = 6$ (**b, e**) and $n = 4$ (**f**) biological replicates in each experimental group. Data are mean \pm s.e.m. Statistics were assessed by two-tailed Student's *t*-test (paired (**a**), or not paired (**b, f**)) or by non-parametric one-way ANOVA (Kruskal–Wallis test) (**d, e, g**); not significant (not indicated), $P > 0.05$; * $P < 0.05$; ** $P < 0.01$; *** $P < 0.001$.

T cell responses in nutrient-deprived environments, and this may be relevant in the context of severe viral infections.

Nutritional ketosis promotes antiviral immunity

T cells in severely ill patients with COVID-19 have been described as containing dysfunctional mitochondria^{39,40}. Our bioenergetic analysis and tracing experiments suggest that BHB is crucial to support mitochondrial function during viral infections. Flow cytometric analysis revealed that CD4⁺ and CD8⁺ T cells from the blood and BALF of patients with COVID-19 ARDS had high levels of PD-1 expression, a sign of potential exhaustion and dysfunction (Extended Data Fig. 8a). To gain insight into the metabolic features of T cells in COVID-19 ARDS, we used SCENITH to analyse a subgroup of patients with COVID-19. T cells in the BALF and blood of individuals with SARS-CoV-2-driven ARDS exhibited a significantly altered metabolic profile towards glycolysis, with a concomitant reduction in mitochondrial dependence (Fig. 4a and

Extended Data Fig. 8b). In addition, we observed that although BALF T cells shifted their metabolic dependence towards glucose, T cells in the blood of individuals with COVID-19 ARDS still showed a residual capacity to oxidize fatty acids and amino acids (Fig. 4a and Extended Data Fig. 8b). Owing to the reduced amounts of BHB and amino acids available in COVID-19 (Figs. 1b and 3c), this capacity might not be sufficient to sustain mitochondrial function. Because we and others have shown that mitochondrial respiration is required for the maintenance of T_H1 cell function⁴¹, these results offer a potential explanation for defective adaptive immune responses in severe COVID-19.

We therefore hypothesized that supplementing BHB through a ketogenic diet consisting of a 4:1 ratio of fat to proteins and carbohydrates^{42,43} could reprogram the metabolism of CD4⁺ T cells, thereby increasing their functionality in severe pulmonary viral infections. Feeding mice a ketogenic diet increased the amounts of BHB in circulation and in lung tissue (Extended Data Fig. 8c). In line with our *in vitro* data, we observed an increase in the percentage and total number of IFN γ ⁺

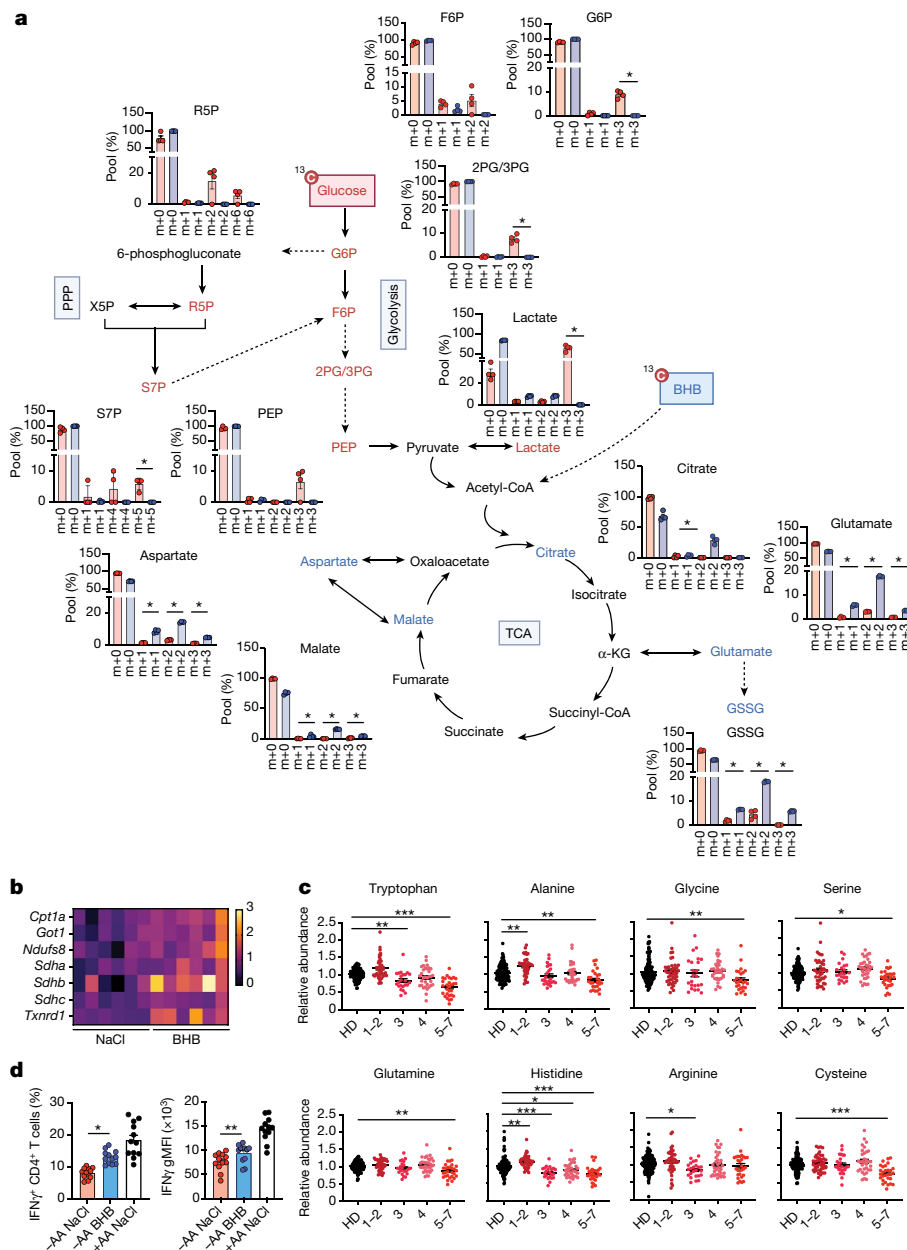


Fig. 3 | BHB is a carbon source for the TCA cycle and amino acid metabolism in T cells. a, Splenic mouse CD4 $^+$ T cells were cultured in T $_H$ 1 polarizing conditions for three days, in the presence or absence of 5 mM BHB, and incubated in 13 C-glucose medium for the last 3 h, or in 13 C-BHB medium for the last 12 h. Pentose phosphate pathway (PPP) and glycolytic or Krebs cycle metabolites were analysed by mass spectrometry. m+0, unlabelled mass of isotope; m+n, native metabolite mass + number of isotopically labelled carbons. F6P, fructose 6-phosphate; G6P, glucose 6-phosphate; R5P, ribose 5-phosphate; X5P, xylulose 5-phosphate; S7P, sedoheptulose 7-phosphate; 2PG/3PG, glyceraldehyde 2- or 3-phosphate; PEP, phosphoenolpyruvate; α -KG, α -ketoglutarate. **b**, Heat map showing the fold change of gene expression for enzymes that regulate cellular metabolic pathways. **c**, Relative abundance of

the indicated amino acids in the serum of patients with COVID-19. HD, healthy donors; 1-7, World Health Organization disease severity score. Data are from a published metabolomic dataset³⁶. **d**, Human CD4 $^+$ T cells were isolated from the blood of healthy donors ($n = 12$) and cultured for one week in T $_H$ 1 polarizing conditions, with or without amino acid (AA) and 5 mM BHB. Percentage of IFN γ CD4 $^+$ T cells and IFN γ gMFI analysed by flow cytometry. Results in **a** are from $n = 5$ pooled mice for each data point ($n = 4$). Data in **b** are representative of three independent experiments with $n = 6$ biological replicates in each experimental group. (**c,d**). Each dot represents a donor³⁶. Data are mean \pm s.e.m. Statistics were assessed by two-tailed Student's *t*-test (**a**) or by non-parametric one-way ANOVA (Kruskal-Wallis test) (**c,d**); not significant (not indicated), $P > 0.05$; * $P < 0.05$; ** $P < 0.01$; *** $P < 0.001$.

CD4 $^+$ T cells, which was accompanied by a concomitant reduction of PD-1 in CD4 $^+$ T cells of IAV-infected mice that were fed a ketogenic diet (Fig. 4b and Extended Data Fig. 8d). Furthermore, supplying mice with a ketogenic diet resulted in a metabolic reprogramming of lung CD4 $^+$ T cells towards OXPHOS and a reduction in their glycolytic capacity (Fig. 4c). Consistently with human BALF (Fig. 4a), we also found increased glucose dependence in lung CD4 $^+$ T cells of infected mice (Fig. 4c). A

ketogenic diet also decreased glucose dependence in favour of the capacity to oxidize amino acids and fatty acids. Transcriptional and protein analysis revealed that a ketogenic diet downmodulated transcripts (Fig. 4d) and proteins that are associated with fibrosis and tissue remodelling (Fig. 4e), supporting the notion that increases of BHB and IFN γ are related to attenuated fibrosis. A ketogenic diet also led to reduced lung damage (total protein in BALF) (Fig. 4f), accelerated viral clearance

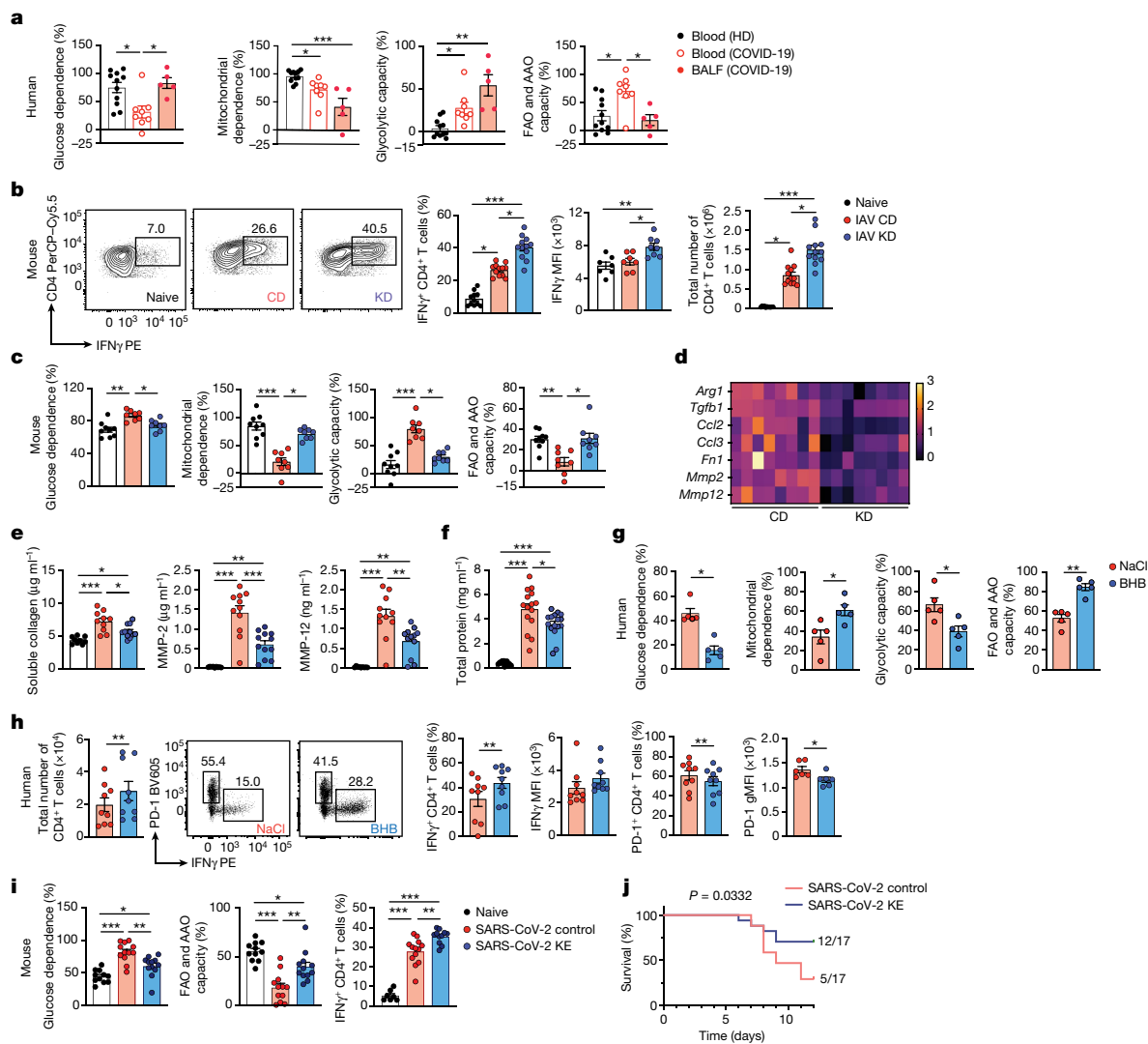


Fig. 4 | BHB rescues the metabolism and function of T cells in severe viral infections. **a**, Analysis of CD4⁺ T cells by SCENITH in the blood of healthy donors (HD; *n* = 11) and in the blood (*n* = 8) or BALF (*n* = 5) of patients with COVID-19 ARDS. **b–f**, C57BL/6 mice were fed a control diet (CD) or a ketogenic diet (KD) for seven days, infected with IAV, euthanized and analysed on day 10. **b**, Representative flow plots, percentage and total number of IFN γ ⁺ CD4⁺ T cells (*n* = 12 in each group; naive *n* = 11), IFN γ gMFI (*n* = 7 naive and CD; *n* = 8 KD), **c**, Analysis by SCENITH of lung CD4⁺ T cells (*n* = 9 naive; *n* = 8 CD and KD). **d**, Expression of fibrotic genes from BALF cells (*n* = 8 in each group). **e**, Soluble collagen (*n* = 9 naive, *n* = 10 CD, *n* = 11 KD) and MMPs (*n* = 9 naive, *n* = 10 CD and *n* = 11 KD). **f**, Total protein (*n* = 13 naive, *n* = 15 CD and *n* = 16 KD). **g, h**, CD4⁺ T cells were isolated from the blood of patients with COVID-19 ARDS and cultured under T_H1 conditions, with or without 5 mM BHB. **g**, Analysis by SCENITH (*n* = 5).

h, Total number of CD4⁺ T cells and percentage of IFN γ ⁺ and PD-1⁺ CD4⁺ T cells (*n* = 9). IFN γ (*n* = 9) and PD-1 gMFI (*n* = 6) assessed by flow cytometry. **i, j**, K18-hACE2 mice were infected with SARS-CoV-2 and euthanized on day 8. Mice were supplied with drinking water (control) or water supplemented with ketone ester (KE). **i**, Analysis of CD4⁺ T cells by SCENITH (*n* = 11 naive; *n* = 12 Ctrl and KE) and percentage of IFN γ ⁺ CD4⁺ T cells (*n* = 7 naive, *n* = 13 control and *n* = 11 KE). **j**, Per cent survival of SARS-CoV-2-infected mice (*n* = 17 in each group). In **a, g, h**, each dot represents one donor. Data are pooled from three (**b–e**), four (**f, i**) or five (**j**) independent experiments. Data are mean \pm s.e.m. Statistics were assessed by non-parametric one-way ANOVA (Kruskal–Wallis test) (**a**), ordinary one-way ANOVA (Tukey’s correction) (**b–f, i**), two-tailed Student’s *t*-test (**g, h**) or log-rank test (Mantel–Cox) (**j**); not significant (not indicated), **P* < 0.05; ***P* < 0.01; ****P* < 0.001.

(Extended Data Fig. 8e) and recovery from weight loss (Extended Data Fig. 8f). A reduction in total protein and fibrosis-associated proteins in BALF, as well as a decrease in collagen deposition, tissue density and lung injury score, indicated a faster resolution of inflammation in mice that were fed a ketogenic diet (Extended Data Fig. 8g–i). Furthermore, increasing the availability of circulating BHB by supplying esterified BHB in the drinking water⁴⁴ (Extended Data Fig. 9a,b) enhanced the responses of T_H1 cells (Extended Data Fig. 9c), while reducing lung damage (Extended Data Fig. 9d) and the expression of genes and proteins associated with fibrosis in IAV-infected mice (Extended Data Fig. 9e,f). Treatment with ketone ester also diminished the dependency of CD4⁺ T cells on glucose but promoted their potential to oxidize amino acids and fatty acids (Extended Data Fig. 9g). Furthermore, treatment with

BHB resulted in improved mitochondrial functionality and oxidation of fatty acids and amino acids, concomitantly leading to a reduction in glycolysis in CD4⁺ T cells from patients with severe COVID-19 (Fig. 4g). Although these T cells exhibited substantial expression of PD-1 *ex vivo* (Extended Data Fig. 8a) and *in vitro* (Fig. 4h), treatment with BHB increased the number of CD4⁺ T cells and the production of IFN γ , but decreased the expression of PD-1 (Fig. 4h). Delivery of ketone ester in a preclinical model of SARS-CoV-2 infection in K18-hACE2 mice⁴⁵ reduced the dependence on glucose but enhanced the potential of CD4⁺ T cells to oxidize amino acids and fatty acids, increasing their production of IFN γ and viral clearance (Fig. 4i, j and Extended Data Fig. 10a). Moreover, ketone ester promoted a faster recovery from weight loss and reduced lung injury, resulting in improved overall survival (Extended

Data Fig. 10b,c). Altogether, our data corroborate the link between infection-induced impaired ketogenesis and dysfunctional CD4⁺ T cell immunity by showing that restoration of BHB supports the functionality of type 1 immune responses in viral infection.

Discussion

Here we show that SARS-CoV-2-induced immune dysregulation correlated with an attenuated increase in BHB in the circulation, which indicates that infection-induced ketogenesis is impaired in COVID-19 but not in influenza ARDS. Although the underlying reasons for this disparity are yet to be determined, we show that BHB substantially boosts the antiviral immune response by promoting the production of IFN γ and the survival of human and mouse CD4⁺ T cells. In COVID-19 ARDS, T cells are exhausted and skewed towards glycolysis, probably as a result of reduced oxygenation of the pulmonary tissue⁴⁶. BHB not only rewires T cells to OXPHOS by fuelling the TCA cycle, but also promotes the synthesis of amino acids that are depleted in COVID-19 ARDS³⁶. Consequently, impaired ketogenesis and production of BHB in COVID-19 ARDS may be at the root of the metabolic dysregulation and defective effector function of T cells, and may predispose patients to pulmonary pathology, including fibrosis. Indeed, lower serum concentrations of IFN γ in patients with COVID-19 have been linked to an increased risk of developing pulmonary fibrosis⁴⁷. Our results thus indicate that an additional mechanism beyond immune overactivation underlies severe COVID-19 pathology⁴⁶. We reveal ketogenesis as a metabolic program that promotes type 1 immunity and prevents the pathogenic remodeling of the airway epithelial tissue. Although, therapeutic (as opposed to prophylactic) relevance has yet to be assessed, our discovery highlights the potential of BHB and a ketogenic diet as a broadly applicable treatment to enhance functional T cell responses in nutrient-deprived environments, which are commonly observed in the context of infections but also tumour growth. In summary, our study establishes a better understanding of how dysregulated host metabolic adaptations to infections may contribute to poor outcomes in COVID-19.

Online content

Any methods, additional references, Nature Research reporting summaries, source data, extended data, supplementary information, acknowledgements, peer review information; details of author contributions and competing interests; and statements of data and code availability are available at <https://doi.org/10.1038/s41586-022-05128-8>.

1. Troha, K. & Ayres, J. S. Metabolic adaptations to infections at the organismal level. *Trends Immunol.* **41**, 113–125 (2020).
2. Wilhelm, C., Surendar, J. & Karagiannis, F. Enemy or ally? Fasting as an essential regulator of immune responses. *Trends Immunol.* **42**, 389–400 (2021).
3. Rao, S. et al. Pathogen-mediated inhibition of anorexia promotes host survival and transmission. *Cell* **168**, 503–516 (2017).
4. Puchalska, P. & Crawford, P. A. Multi-dimensional roles of ketone bodies in fuel metabolism, signaling, and therapeutics. *Cell Metab.* **25**, 262–284 (2017).
5. Wang, A. et al. Opposing effects of fasting metabolism on tissue tolerance in bacterial and viral inflammation. *Cell* **166**, 1512–1525 (2016).
6. Medzhitov, R., Schneider, D. S. & Soares, M. P. Disease tolerance as a defense strategy. *Science* **335**, 936–941 (2012).
7. Ayres, J. S. Immunometabolism of infections. *Nat. Rev. Immunol.* **20**, 79–80 (2020).
8. Guan, W. J. et al. Clinical characteristics of coronavirus disease 2019 in China. *N. Engl. J. Med.* **382**, 1708–1720 (2020).
9. Zhu, N. et al. A novel coronavirus from patients with pneumonia in China, 2019. *N. Engl. J. Med.* **382**, 727–733 (2020).
10. Fan, E. et al. COVID-19-associated acute respiratory distress syndrome: is a different approach to management warranted? *Lancet Respir. Med.* **8**, 816–821 (2020).
11. Zheng, H. Y. et al. Elevated exhaustion levels and reduced functional diversity of T cells in peripheral blood may predict severe progression in COVID-19 patients. *Cell. Mol. Immunol.* **17**, 541–543 (2020).
12. Steinert, E. M., Vasan, K. & Chandel, N. S. Mitochondrial metabolism regulation of T cell-mediated immunity. *Annu. Rev. Immunol.* **39**, 395–416 (2021).
13. Stefan, N., Birkenfeld, A. L. & Schulze, M. B. Global pandemics interconnected—obesity, impaired metabolic health and COVID-19. *Nat. Rev. Endocrinol.* **17**, 135–149 (2021).
14. Zhu, L. et al. Association of blood glucose control and outcomes in patients with COVID-19 and pre-existing type 2 diabetes. *Cell Metab.* **31**, 1068–1077 e1063 (2020).
15. Del Valle, D. M. et al. An inflammatory cytokine signature predicts COVID-19 severity and survival. *Nat. Med.* **26**, 1636–1643 (2020).
16. Merad, M. & Martin, J. C. Pathological inflammation in patients with COVID-19: a key role for monocytes and macrophages. *Nat. Rev. Immunol.* **20**, 355–362 (2020).
17. Huang, C. et al. Clinical features of patients infected with 2019 novel coronavirus in Wuhan, China. *Lancet* **395**, 497–506 (2020).
18. Kox, M., Waalders, N. J. B., Kooistra, E. J., Gerretsen, J. & Pickkers, P. Cytokine levels in critically ill patients with COVID-19 and other conditions. *J. Am. Med. Assoc.* **324**, 1565–1567 (2020).
19. Sinha, P., Matthay, M. A. & Calfee, C. S. Is a “cytokine storm” relevant to COVID-19? *JAMA Intern. Med.* **180**, 1152–1154 (2020).
20. Wendisch, D. et al. SARS-CoV-2 infection triggers profibrotic macrophage responses and lung fibrosis. *Cell* **184**, 6243–6261 (2021).
21. Chen, Z. & John Wherry, E. T cell responses in patients with COVID-19. *Nat. Rev. Immunol.* **20**, 529–536 (2020).
22. Grifoni, A. et al. Targets of T cell responses to SARS-CoV-2 coronavirus in humans with COVID-19 disease and unexposed individuals. *Cell* **181**, 1489–1501 (2020).
23. Rydzynski Moderbacher, C. et al. Antigen-specific adaptive immunity to SARS-CoV-2 in acute COVID-19 and associations with age and disease severity. *Cell* **183**, 996–1012 (2020).
24. Sekine, T. et al. Robust T Cell immunity in convalescent individuals with asymptomatic or mild COVID-19. *Cell* **183**, 158–168 (2020).
25. Braun, J. et al. SARS-CoV-2-reactive T cells in healthy donors and patients with COVID-19. *Nature* **587**, 270–274 (2020).
26. Tan, A. T. et al. Early induction of functional SARS-CoV-2-specific T cells associates with rapid viral clearance and mild disease in COVID-19 patients. *Cell Rep.* **34**, 108728 (2021).
27. Zhao, J. et al. Airway memory CD4⁺ T cells mediate protective immunity against emerging respiratory coronaviruses. *Immunity* **44**, 1379–1391 (2016).
28. Goldberg, E. L. et al. Ketogenic diet activates protective $\gamma\delta$ T cell responses against influenza virus infection. *Sci. Immunol.* **4**, eaav2026 (2019).
29. Ryu, S. et al. Ketogenic diet restrains aging-induced exacerbation of coronavirus infection in mice. *eLife* **10**, e66522 (2021).
30. Zhang, H. et al. Ketogenesis-generated β -hydroxybutyrate is an epigenetic regulator of CD8⁺ T-cell memory development. *Nat. Cell Biol.* **22**, 18–25 (2020).
31. Hirschberger, S. et al. Very-low-carbohydrate diet enhances human T-cell immunity through immunometabolic reprogramming. *EMBO Mol. Med.* **13**, e14323 (2021).
32. Arguello, R. J. et al. SCENITH: a flow cytometry-based method to functionally profile energy metabolism with single-cell resolution. *Cell Metab.* **32**, 1063–1075 (2020).
33. Desdin-Mico, G. et al. T cells with dysfunctional mitochondria induce multimorbidity and premature senescence. *Science* **368**, 1371–1376 (2020).
34. Keating, S. E. et al. Metabolic reprogramming supports IFN- γ production by CD56^{bright} NK cells. *J. Immunol.* **196**, 2552–2560 (2016).
35. Franchina, D. G., Dostert, C. & Brenner, D. Reactive oxygen species: involvement in T cell signaling and metabolism. *Trends Immunol.* **39**, 489–502 (2018).
36. Su, Y. et al. Multi-omics resolves a sharp disease-state shift between mild and moderate COVID-19. *Cell* **183**, 1479–1495 (2020).
37. Thomas, T. et al. COVID-19 infection alters kynurenine and fatty acid metabolism, correlating with IL-6 levels and renal status. *JCI Insight* **5**, e140327 (2020).
38. Ma, E. H. et al. Serine is an essential metabolite for effector T cell expansion. *Cell Metab.* **25**, 482 (2017).
39. Thompson, E. A. et al. Metabolic programs define dysfunctional immune responses in severe COVID-19 patients. *Cell Rep.* **34**, 108863 (2021).
40. Siska, P. J. et al. Metabolic imbalance of T cells in COVID-19 is hallmarked by basigin and mitigated by dexamethasone. *J. Clin. Invest.* **131**, e148225 (2021).
41. Pearce, E. L., Poffenberger, M. C., Chang, C. H. & Jones, R. G. Fueling immunity: insights into metabolism and lymphocyte function. *Science* **342**, 1242454 (2013).
42. Lutas, A. & Yellen, G. The ketogenic diet: metabolic influences on brain excitability and epilepsy. *Trends Neurosci.* **36**, 32–40 (2013).
43. Kennedy, A. R. et al. A high-fat, ketogenic diet induces a unique metabolic state in mice. *Am. J. Physiol. Endocrinol. Metab.* **292**, E1724–E1739 (2007).
44. Cox, P. J. et al. Nutritional ketosis alters fuel preference and thereby endurance performance in athletes. *Cell Metab.* **24**, 256–268 (2016).
45. Winkler, E. S. et al. SARS-CoV-2 infection of human ACE2-transgenic mice causes severe lung inflammation and impaired function. *Nat. Immunol.* **21**, 1327–1335 (2020).
46. Osuchowski, M. F. et al. The COVID-19 puzzle: deciphering pathophysiology and phenotypes of a new disease entity. *Lancet Respir. Med.* **9**, 622–642 (2021).
47. Hu, Z. J. et al. Lower circulating interferon-gamma is a risk factor for lung fibrosis in COVID-19 patients. *Front. Immunol.* **11**, 585647 (2020).

Publisher's note Springer Nature remains neutral with regard to jurisdictional claims in published maps and institutional affiliations.

Springer Nature or its licensor holds exclusive rights to this article under a publishing agreement with the author(s) or other rightsholder(s); author self-archiving of the accepted manuscript version of this article is solely governed by the terms of such publishing agreement and applicable law.

© The Author(s), under exclusive licence to Springer Nature Limited 2022

Bonn COVIMMUNE Consortium

Christoph Wilhelm^{1,6}, **Christian Bode**^{2,16}, **Christian Putensen**², **Zeinab Abdullah**¹¹, **Natalio Garbi**¹¹, **Eicke Latz**¹², **Susanne Schmidt**¹², **Gunther Hartmann**¹³, **Hendrik Streeck**¹⁴ & **Beate M. Kümmerer**¹⁴

¹²Institute of Innate Immunity, Medical Faculty, University Hospital Bonn, University of Bonn, Bonn, Germany. ¹³Institute of Clinical Chemistry and Clinical Pharmacology, Medical Faculty, University Hospital Bonn, University of Bonn, Bonn, Germany. ¹⁴Institute of Virology, Medical Faculty, University Hospital Bonn, University of Bonn, Bonn, Germany.

Methods

Mice

C57BL/6 (wild-type) and K18-hACE2 transgenic (K18-hACE2) mice were bred in-house or purchased from Charles River or The Jackson Laboratory and maintained at in-house facilities. All mice were kept under specific-pathogen-free conditions. All procedures were performed according to ethical protocols approved by the ethics committee of North Rhine-Westphalia. All mice used were male and female between 6 and 20 weeks of age. Mice were randomly assigned to the control and ketogenic diet groups or to the control and ketone ester groups. Animal experiments were not done in a blinded manner as the investigators needed to design and conduct experiments and analyse the data.

Isolation of cells from blood and tissue samples

Serum samples from patients with moderate COVID-19 or ARDS due to influenza, COVID-19 or bacterial pneumonia were obtained from University Hospital Bonn ($n = 79$), Radboud University Medical Center Nijmegen ($n = 35$), University Hospital Essen ($n = 21$) and Hannover Medical School ($n = 20$). ARDS was defined according to the Berlin definition. Blood from healthy donors and BALF samples were collected at the University Hospital Bonn. Informed consent was obtained from all patients and protocols were approved by the institutional review board of each hospital. Isolation of peripheral blood mononuclear cells (PBMCs) and single-cell suspensions was performed using Ficoll Paque Plus (Millipore Sigma) density gradient centrifugation. Serum was collected from each patient and donor and used for the isolation of RNA and quantification of cytokines. Before fluorescence-activated cell sorting (FACS) analysis, BALF samples were collected, washed and fixed with 4% paraformaldehyde, and lysis of red blood cells with ammonium-chloride-potassium (ACK) lysing buffer was performed for blood samples according to the manufacturer's instructions.

Multiplex quantification of cytokines, hormones and fibrosis markers

Concentrations of cytokines, hormones, pro-fibrotic proteins, total protein and collagen were measured in the serum and in BALF samples from patients by multiplex immunoassay analysis (Luminex (R&D) using the Luminex xPONENT software (Thermo Fisher Scientific) and Legendplex (BioLegend)), bicinchoninic acid assay (total protein) or Sircol soluble collagen assay (collagen) according to the manufacturer's instructions.

Histology

The left lung lobe was fixed in 10% formaldehyde solution and embedded into paraffin blocks. Sections were stained with picosirius red to assess collagen deposition using the ZEN 3.1 blue edition (ZEISS). The area of collagen fibres as a function of their colour hue was quantified using polarized light microscopy as previously described⁴⁸. According to a previously published protocol⁴⁹, an adapted algorithm was created with MATLAB software (MathWorks). The algorithm transformed all images from RGB to the HSV colour model. The red colour component was separated as a function of 2–9 and 230–256. Collagen content was quantified as the area of red of each image. The green channel of RGB images from picosirius-red-stained lung sections was binarized with MATLAB software as previously reported⁵⁰ to quantify the infiltrates. Black pixels were counted, and the density was shown as pixel count per image. Calculation of the lung injury score was determined as previously described^{51,52}. In brief, two blinded investigators evaluated the sum of histological evidence of leukocyte influx in both alveolar and interstitial spaces, proteinaceous debris, formation of hyaline membranes and alveolar septal thickening, then weighted the variables according to their relevance in reflecting the lung damage. Subsequently, variables were normalized to four evaluated fields of

haematoxylin and eosin (H&E)-stained (Sigma-Aldrich) lung sections of mice infected with SARS-CoV-2 or influenza A/Puerto Rico/8/1934 virus.

RNA isolation, library construction, sequencing and analysis

After the isolation of RNA, 100 ng total RNA was used for library preparation using the QuantSeq 3' mRNA-Seq Library Prep kit (Lexogen) according to the manufacturer's instructions. Afterwards, samples were subjected to sequencing on a NovaSeq 6000 sequencer (Illumina) with 1 × 100 bp single-end reads and a mean coverage of 10 million raw reads per sample. Data were analysed by Qlucore software (<https://qlucore.com/>).

Infection with influenza A virus

C57BL/6 mice were anaesthetized with isoflurane and infected intranasally with 5×10^3 plaque-forming units (PFU) of influenza A/Puerto Rico/8/1934 virus in 50 μ l PBS on day 0. Mice were euthanized on day 4, 7 or 10 after infection, BALF was collected and the lungs were removed for further analysis. Lung homogenate was obtained by meshing diced lung fragments through a 40- μ m cell strainer, and the cell-free supernatant was stored at -80°C for cytokine analysis. A piece of the lung and the liver tissues were placed in RNA later buffer and stored at -80°C for subsequent RNA extraction and qRT-PCR analysis.

Infection with SARS-CoV-2

K18-hACE2 mice were anaesthetized with ketamine-xylazine and infected intranasally with 60 PFU SARS-CoV-2 (clinical isolate of wild-type strain) in 30 μ l PBS on day 0. Mice reached the clinical end-point after the loss of 25% or of 20% of their initial starting weight for more than two consecutive days. Mice were euthanized on day 8 after infection, BALF was collected and the lungs were removed for further analysis. A piece of the lung and the liver tissues were placed in Trizol and stored at -80°C for subsequent RNA extraction and qRT-PCR analysis.

Preparation of cell suspensions from lung tissue

Lung tissues were diced and digested with 0.25 mg ml⁻¹ Liberase TL (Roche) and 1 mg ml⁻¹ DNase I (Sigma) at 37 °C for 1 h. Isolated lung cells were further purified using a 37.5% Percoll gradient, followed by lysis of red blood cells with ACK lysing buffer.

Measurement of glucose and ketone bodies

Concentrations of glucose and BHB in the plasma and lung homogenate were measured by using an ACCU-CHECK Aviva (Roche) and a FreeStyle Precision Neo H instrument (Abbott), respectively.

Flow cytometry of human and mouse single-cell suspensions

Cells were stained with surface antibodies and Fixable Viability Dye (Zombie UV, BioLegend) in PBS containing 2% fetal calf serum (FCS) (FACS buffer) for 30 min at 4 °C in the presence of human (BioLegend) or mouse (BioXcell) Fc block. For experiments involving intracellular staining of cytokines, T cells were stimulated for 3 h (mouse) and 6 h (human) with phorbol 12-myristate 13-acetate (PMA; 50 ng ml⁻¹) (BioGems) and ionomycin (1 μ g ml⁻¹) (BioGems) in the presence of brefeldin A (1 μ g ml⁻¹) (GolgiPlug, BD Biosciences). Cells were washed with FACS buffer followed by fixation with the Foxp3 fixation/permeabilization kit (eBioscience) in accordance with the manufacturer's instructions, and stained with intracellular antibodies for 60 min at 4 °C.

Mouse surface and intracellular antibodies

Single-cell suspension was stained with anti-CD16/32 (BioXcell, 1 mg ml⁻¹, 1:100) and conjugated antibodies against any combination of the following surface antigens: CD4 (RM4.5, 1:400), CD8 (53-6.7, 1:400), CD45 (30-F11, 1:400), TCR β (H57-597, 1:200) and PD-1 (29F.1A12, 1:200). For examination of cytokines and cellular proliferation, conjugated

antibodies against any combination of the following intracellular antigens were used: TNF (MP6-X122, 1:200), IFN γ (XMGL1.2, 1:200) and Ki-67(16A8, 1:1,000).

Human surface and intracellular antibodies

Cells were stained with Human TruStain FcXTM (BioLegend, 1:100) conjugated antibodies against any combination of the following surface antigens: CD4 (RPA-T4, 1:200), CD8 (SK1, 1:200), CD45 (HI30; 1:400) and PD-1 (EH12.2H7; 1:200). For examination of cytokines and cellular proliferation, the following antibodies were used: TNF (MAB11, 1:200), IFN γ (4S.B3, 1:200) and Ki-67 (Ki-67, 1:400).

Purification and culturing of human CD4⁺ T cells and CD8⁺ T cells

CD4⁺ T cells or CD8⁺ T cells were purified from PBMCs using magnetic positive selection with biotin human anti-CD4 or anti-CD8 antibodies, respectively, followed by incubation with streptavidin-coupled magnetic microbeads (BioLegend) and positive selection with magnets. Purity was assessed by flow cytometry on a BD LSRFortessa using anti-CD4 (RPA-T4, 1:400) antibodies and anti-CD8 (RPA-T8, 1:400) antibodies. Cells were plated on 48-well plates, coated with anti-CD3 (1 μ g ml⁻¹) and anti-CD28 (10 μ g ml⁻¹) antibodies, in RPMI medium or DMEM, supplemented with 10% FCS, penicillin, streptomycin, HEPES, glutamine, pyruvate, nonessential amino acids and β -mercaptoethanol diluted with PBS (1:1), in the presence of IL-2 (10 ng ml⁻¹, Peprotech) and IL-12 (10 ng ml⁻¹, Peprotech) (T_H1 conditions), with or without amino acids. Human CD4⁺ T cell cultures were supplemented on days 0, 1 and 2 with 5 mM NaCl or 5 mM BHB and collected after 6 days of culture. Cultured cells were stimulated for 6 h with PMA (50 ng ml⁻¹) (BioGems) and ionomycin (1 μ g ml⁻¹) (BioGems) in the presence of brefeldin A (1 μ g ml⁻¹) (GolgiPlug, BD Biosciences), stained for viability (Zombie UV Fixable Viability Dye (BioLegend)) and surface markers, fixed and permeabilized with 3.7% formaldehyde (Sigma) and 0.1% NP-40, respectively, and stained for intracellular cytokines.

Purification and culturing of mouse CD4⁺ T cells and CD8⁺ T cells

Naive CD4⁺ T cells or CD8⁺ T cells were purified from mouse spleens using the magnetic negative selection kit (Mojosort mouse CD4 naive T cell isolation kit, BioLegend; CD8⁺ T cell isolation kit, Miltenyi) according to the manufacturer's instructions. Purity was assessed by flow cytometry on a BD LSRFortessa Flow Cytometer using anti-mouse CD4 (RM4-5, 1:400) and anti-mouse CD8 (Ly-3, 1:400) antibodies. Cells were plated on 48-well plates, coated with anti-CD3 (1 μ g ml⁻¹) and anti-CD28 (10 μ g ml⁻¹) antibodies, in RPMI medium supplemented with 10% FCS, penicillin, streptomycin, HEPES, glutamine, pyruvate, nonessential amino acids and β -mercaptoethanol diluted with PBS (1:1) in the presence of IL-12 (3 ng ml⁻¹, Peprotech) (T_H1 conditions). Cultures were supplemented on days 0, 1 and 2 with 5 mM NaCl or 5 mM BHB. Mouse CD4⁺ T cells were collected at days 3 and 6 of culture. Viability was assessed by Zombie UV Fixable Viability Dye (BioLegend) and cytokine production was measured by intracellular cytokine staining after 3 h stimulation with PMA (50 ng ml⁻¹) (BioGems) and ionomycin (1 μ g ml⁻¹) (BioGems) in the presence of brefeldin A (1 μ g ml⁻¹) (GolgiPlug, BD Biosciences). Cells were stained for viability and surface markers, fixed with 3.7% formaldehyde (Sigma), permeabilized with 0.1% NP-40 and stained for intracellular cytokines.

In vitro tracing of ¹³C-labelled glucose and BHB

Splenic mouse CD4⁺ T cells were activated in culture for three days. Cells were washed and incubated for 3 h with 5 mM of ¹³C-labelled glucose at 37 °C in glucose-free medium or for 12 h with 5 mM of ¹³C-labelled BHB. After culture, around 2 million cells were washed with calcium- and magnesium-free Hanks' balanced salt solution (HBSS). Liquid chromatography–mass spectrometry detection included one-step organic solvent extraction of cells, and separation on a 1 mm \times 150-mm HILIC specific column in a 35-min cycle. Isotope enrichment of targeted

metabolites was corrected for natural abundance and reported as a ratio of M, M+1, M+2, M+3 and so on (MassHunter Profinder software). The extraction, run and final analyses were done by Creative Proteomics.

In vivo and ex vivo tracing of ¹³C-labelled BHB

C57BL/6 mice were anaesthetized with isoflurane and infected intranasally with 5 \times 10³ PFU of IAV in 50 μ l PBS on day 0. For the in vivo tracing experiment, 300 mM ¹³C-labelled BHB (Eurisotop) was injected intraperitoneally for 20 min on day 7 before euthanizing the mice. Lung tissue was diced and digested with 0.25 mg ml⁻¹ Liberase TL (Roche) and 1 mg ml⁻¹ DNase I (Sigma) at 37 °C for 20 min. Isolated lung cells were further purified using a 28% Percoll gradient, followed by lysis of red blood cells with ACK lysing buffer. CD4⁺ T cells were purified using the magnetic negative selection kit (Mojosort mouse CD4 T cell isolation kit, BioLegend) following the manufacturer's instructions. For ex vivo tracing experiments, CD4⁺ T cells isolated from untreated mice were further cultured for 2 h in diluted medium with ¹³C-labelled BHB. Purity and cell death was assessed by flow cytometry on a BD LSRFortessa and cells were pooled to a total of 1.5 \times 10⁶ cells per sample, washed with HBSS and resuspended in methanol. Analyses were performed by gas chromatography–mass spectrometry (GC–MS).

Sample preparation and GC–MS

Samples were prepared and processed as described previously⁵³. Cell pellets (1.0 or 1.5 \times 10⁶ cells) were mixed with 400 or 600 μ l of a methanol and water mixture (1:1; v/v) and 200 or 300 μ l chloroform and subsequently vortexed for 20 min at 1,200 rpm at 4 °C on a thermomixer (Eppendorf) and centrifuged (Eppendorf 5415R) at 17,000g for 5 min at 4 °C. The upper polar phase (200 μ l) was transferred into GC vials and evaporated to complete dryness at 4 °C in a vacuum centrifuge (Labconco Corporation) for at least 3 h. Samples were online derivatized and automatically prepared by a Gerstel MultiPurposeSampler. Derivatization was performed with 15 μ l methoxyamine hydrochloride (Sigma-Aldrich) in pyridine (20 mg ml⁻¹) at 55 °C for 30 min followed by 15 μ l *N*-methyl-*N*-(tert-butyl)dimethylsilyl trifluoroacetamide (Macherey Nagel) for 90 min at 55 °C. GC–MS measurements were performed on a combined set-up of a 7890B GC with a 5977B MSD (Agilent Technologies). A 30-m DB-35ms capillary column (inner diameter, 250 μ m; film, 0.25 μ m) and 5-m DuraGuard capillary in front of the analytical column (Agilent J&W GC Column) were used for the separation of metabolites. Samples (1 μ l) were injected into the GC inlet at 270 °C and helium was used as a carrier gas (flow rate of 1 ml min⁻¹). The GC oven temperature was held at 80 °C for 6 min and then increased at 6 °C per min until reaching 280 °C and held for 10 min. The electron ionization energy was set to 70 eV. The temperature of the MS source and the quadropole were set, respectively, at 230 °C and 150 °C. Full scan (70–800 *m/z*, 3.9 scans per second) and with a second injection, selective ion chromatograms were recorded for lactate (261, 262, 263, 264, 265, 266, 267; 10 scans per second), citrate (591, 592, 593, 594, 595, 596, 597, 598, 599, 600; 10 scans per second), glutamate (432, 433, 434, 435, 436, 437, 438, 439, 440; 10 scans per second), malate (419, 420, 421, 422, 423, 424, 425, 426; 10 scans per second) and aspartate (418, 419, 420, 421, 422, 423, 424, 425; 10 scans per second). Raw MS data processing, including ion chromatographic deconvolution, peak integration and correction for natural occurring isotopes, was performed with the MetaboliteDetector software.

Metabolic assays

For real-time measurement of the oxygen consumption rate (OCR) and extracellular acidification rate (ECAR), 2 \times 10⁵ in-vitro-polarized T_H1 cells were washed with Seahorse XF RPMI medium (pH 7.4) supplemented with 5 mM glucose (or without), 1 mM pyruvate, 2 mM glutamine, 100 μ g ml⁻¹ linoleic or oleic acid and 5 mM NaCl or BHB, respectively. Quadruplicates were seeded in poly-L-lysine (0.01%)

Article

pre-coated Seahorse XF96 Cell Culture Microplates and the plate was kept in a non-carbonated incubator for 30 min at 37 °C. Cells were analysed with an XF96 Extracellular Flux Analyzer using the Wave desktop software (Agilent). Three or more consecutive measurements were obtained under basal conditions followed by the addition of 1.5 μM oligomycin, which inhibits the mitochondrial ATP synthase; 1.5 μM FCCP (carbonyl cyanide 4-(trifluoromethoxy)phenylhydrazone), which uncouples ATP synthesis from oxygen consumption; and a combination of 0.5 μM rotenone and antimycin A, which inhibits the electron transport chain by blocking complex I and III, respectively. All chemicals used for these assays were obtained from Agilent. Spare respiratory capacity was calculated as the difference between the basal OCR and the maximal OCR after the addition of FCCP.

CRISPR–Cas9 gene editing of human and mouse naive CD4⁺ T cells
Single-guide RNAs (sgRNAs) targeting human *BDHI* (mC*mC*mG*rUrArC rUrGrC rArUrC rArCrC rArArG rUrUrG rUrUrU rUrArG rArGrC rUrArG rArArA rUrArG rCrArA rGrUrU rArArA rArUrA rArGrG rCrUrA rGrUrC rCrGrU rUrArU rCrArA rCrUrU rGrArA rArArA rGrUrG rGrCrA rCrCrG rArGrU rCrGrG rUrGrC mU*mU*mU*rU) and mouse *Bdh1* (mA*mC*mG*rCrArG rGrCrA rUrCrU rCrArA rCrGrU rUrUrG rUrUrU rUrArG rArGrC rUrArG rArArA rUrArG rCrArA rGrUrU rArArA rArUrA rArGrG rCrUrA rGrUrC rCrGrU rUrArU rCrArA rCrUrU rGrArA rArArA rGrUrG rGrCrA rCrCrG rArGrU rCrGrG rUrGrC mU*mU*mU*rU) were purchased from IDT (m, 2'-O-methyl base; *, phosphorothioate bond; r, ribonucleotide). sgRNA–Cas9 RNPs were formed by incubating 1 μl sgRNA (0.3 nmol μl⁻¹) with 0.6 μl Alt-R.S.p Cas9 Nuclease V3 (10 mg ml⁻¹; IDT) for 10 min at room temperature. Naive CD4⁺ T cells were resuspended in 20 μl P3 buffer (P3 Primary Cell 4D-Nucleofector X Kit S; Lonza), mixed with sgRNA–Cas9 RNPs and electroporated using a Lonza 4D-Nucleofector system (pulse code: EO115 for human CD4⁺ T cells and DN100 for mouse CD4⁺ T cells). Cells were rested for 2 h at 37 °C, divided and transferred to a new plate for further treatment with 5 mM NaCl or 5 mM βOHB.

In vitro inhibitor treatment

To inhibit OXPHOS in human T cells, increasing concentrations of rotenone, antimycin A and oligomycin (10 nM, 100 nM and 1 μM) were used to block the activity of complex I, III and V of the respiratory chain, respectively.

Diet studies

Control diet AIN 93G (17.6% protein, 7.1% fat and 11% sugar) and ketogenic diet TD.130659 (15% protein, 72% fat and 2.4% sugar) were purchased from Ssniff. Mice were placed on ketogenic or control diets one week before infection with IAV and maintained on these experimental diets throughout the experimental study.

Supplementation with ketone ester

Ketone ester (D-β-hydroxybutyrate-(R)-1,3 butanediol monoester) was a gift from K. Clarke. Mice were supplemented with 20 mg ml⁻¹ ketone ester in the drinking water from day 0 of infection with IAV or SARS-CoV-2 for the duration of the experimental study.

qRT–PCR

RNA was extracted from purified T cells or whole BALF cells using Trizol (Thermo Fisher Scientific) and reverse-transcribed with the RevertAid Kit (Thermo Fisher Scientific) according to the manufacturer's instructions. RNA from whole lung or liver tissue was extracted using the Dynabeads mRNA direct kit (Thermo Fisher Scientific) according to the manufacturer's instructions. The cDNA served as a template for amplification of the genes of interest. For analysis of genes expressed, TaqMan probes for human *IFNG*, *IFITM3*, *IFI27*, *IFI44L*, *IFIT1*, *MX1*, *ISG15*, *MX2*, *RSAD2* and *SIGLEC1*, mouse *Ndusf8*, *Sdha*, *Sdhb*, *Sdhc*, *Txnrd1*, *Got1*, *Arg1*, *Tgfb1*, *Ccl2*, *Ccl3*, *Fn1*, *Mmp2* and *Mmp12* or viral *NI* and *N2*

(SARS-CoV-2) (IDT) were used. Analysis of *PBI* (IAV) transcripts was performed with a SYBR Green-based qRT–PCR assay using the following primers: forward: 5'-ACACAAGGCCGACAGACCTA-3' and reverse: 5'-ATGCTGTTGCAGCAGGTTGG-3' and *Actb* (QIAGEN; QT01136772) as the housekeeping gene. Target-gene expression was determined by QuantStudio Real-Time PCR software (Thermo Fisher Scientific) and calculated using the comparative method for relative quantification upon normalization to *HPRT/Hprt* or *18S* gene expression. Analysis of *PBI* (IAV) transcripts was performed with SYBR Green-based qPCR using the following primers: forward: 5'-ACACAAGGCCGACAGACCTA-3' and reverse: 5'-ATGCTGTTGCAGCAGGTTGG-3' and *Actb* (QIAGEN; QT01136772) as the housekeeping gene.

SCENITH

Mouse and human cells were incubated for 30 min at 37 °C, 5% CO₂, followed by treatment for 15 min at 37 °C, 5% CO₂ with control, 2-DG (100 mM; Sigma-Aldrich), oligomycin (1 μM; Sigma-Aldrich) or a combination of both drugs. Puromycin (10 μg ml⁻¹; Abcam) was added for 30 min at 37 °C. After staining with primary antibodies as described above, cells were fixed and permeabilized using the Foxp3 fixation/permeabilization kit (eBioscience), following the manufacturer's instructions. Intracellular staining of puromycin was performed by incubation with the anti-puro monoclonal antibody (1:1,000, cClone MABE343, Merck) for 60 min at 4 °C. This protocol was adapted from the original SCENITH kit (<http://www.scenith.com>) and protocols developed by R. Argüello.

Quantification and statistical analysis

Data were analysed with Prism software (GraphPad). A non-parametric one-way ANOVA (Kruskal–Wallis test) or a two-tailed Student's *t*-test was used for all statistical analyses: not significant (NS) $P > 0.05$; * $P < 0.05$; ** $P < 0.01$; *** $P < 0.001$; **** $P < 0.0001$.

Reporting summary

Further information on research design is available in the Nature Research Reporting Summary linked to this article.

Data availability

Raw RNA-seq files have been deposited in the GEO database under the accession number GSE207077. The metabolomic data were previously published³⁶ and can be obtained from Mendeley Data at <https://doi.org/10.17632/tzydswwhb5.5>. All other data generated or analysed in this study are included in the published Article or its Supplementary Information). Source data are provided with this paper.

48. Faulk, D. M. et al. ECM hydrogel coating mitigates the chronic inflammatory response to polypropylene mesh. *Biomaterials* **35**, 8585–8595 (2014).
49. Whittaker, P., Klöner, R. A., Boughner, D. R. & Pickering, J. G. Quantitative assessment of myocardial collagen with picrosirius red staining and circularly polarized light. *Basic Res. Cardiol.* **89**, 397–410 (1994).
50. Nguyen, D. M. et al. An automated algorithm to quantify collagen distribution in aortic wall. *J. Histochem. Cytochem.* **67**, 267–274 (2019).
51. Matute-Bello, G. et al. An official American Thoracic Society workshop report: features and measurements of experimental acute lung injury in animals. *Am. J. Respir. Cell Mol. Biol.* **44**, 725–738 (2011).
52. Peukert, K. et al. Inhibition of caspase-1 with tetracycline ameliorates acute lung injury. *Am. J. Respir. Crit. Care Med.* **204**, 53–63 (2021).
53. Sapcaru, S. C. et al. Simultaneous extraction of proteins and metabolites from cells in culture. *MethodsX* **1**, 74–80 (2014).

Acknowledgements C.W. was supported by the Deutsche Forschungsgemeinschaft (DFG; German Research Foundation) under Germany's Excellence Strategy (EXC2151, 390873048), a DFG program grant (C.W. and C.B.; BO 3640/2-1/WI 4554/4-1) and the Ministry for Science and Education of the Republic of Germany (COVIMMUNE/O1K120343, BMBF). S.D. is supported by the DFG (DA1209/4-3). M.G.N. was supported by an ERC Advanced Grant (833247) and a Spinoza Grant of the Netherlands Organization for Scientific Research. We thank K. Clarke for providing the ketone ester drink; the animal facility staff for animal care at the University Hospital Bonn (UKB); staff from the UKB flow core facility, A. Dolf, P. Wurst and M. Germer for cell sorting; the bioinformatics core facility, A. Bunes and A. Sahu; the UKB sequencing core facility; M. Lucas, A. Wilhelm and

the Wilhelm laboratory for critical discussions regarding the manuscript; and the COVID Sittich for continuous support.

Author contributions F.K., K. Peukert and L.S. designed and performed the experiments. M.F., C.F., S.S., B.S., S.D., T.W., I.G., A.H.d.N., P.P., M.M.B., T.B. and C.P. collected samples and patient data and performed medical evaluations. J.L.K provided image-processing analysis. M.M., P.W., B.A., N.G., M.G.N., H.K. and P.M. provided experimental help. F.N. and K.H. performed the metabolic-tracing analysis. K. Placek, C.B. and C.W. supervised the experiments and wrote the manuscript. C.B and C.W. supervised the study. Contributions of Bonn COVIMMUNE consortium members: E.L., S.S., Z.A., G.H., H.S. and B.M.K. provided help with the collection of human samples and experimental support.

Competing interests The authors declare no competing interests.

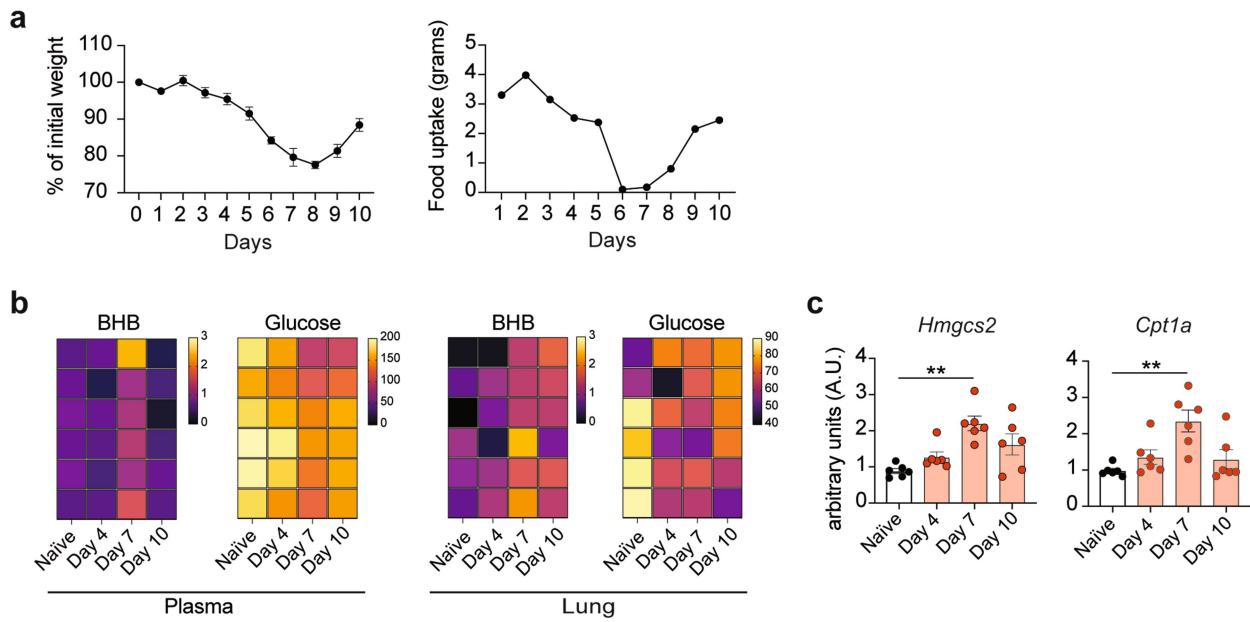
Additional information

Supplementary information The online version contains supplementary material available at <https://doi.org/10.1038/s41586-022-05128-8>.

Correspondence and requests for materials should be addressed to Christian Bode or Christoph Wilhelm.

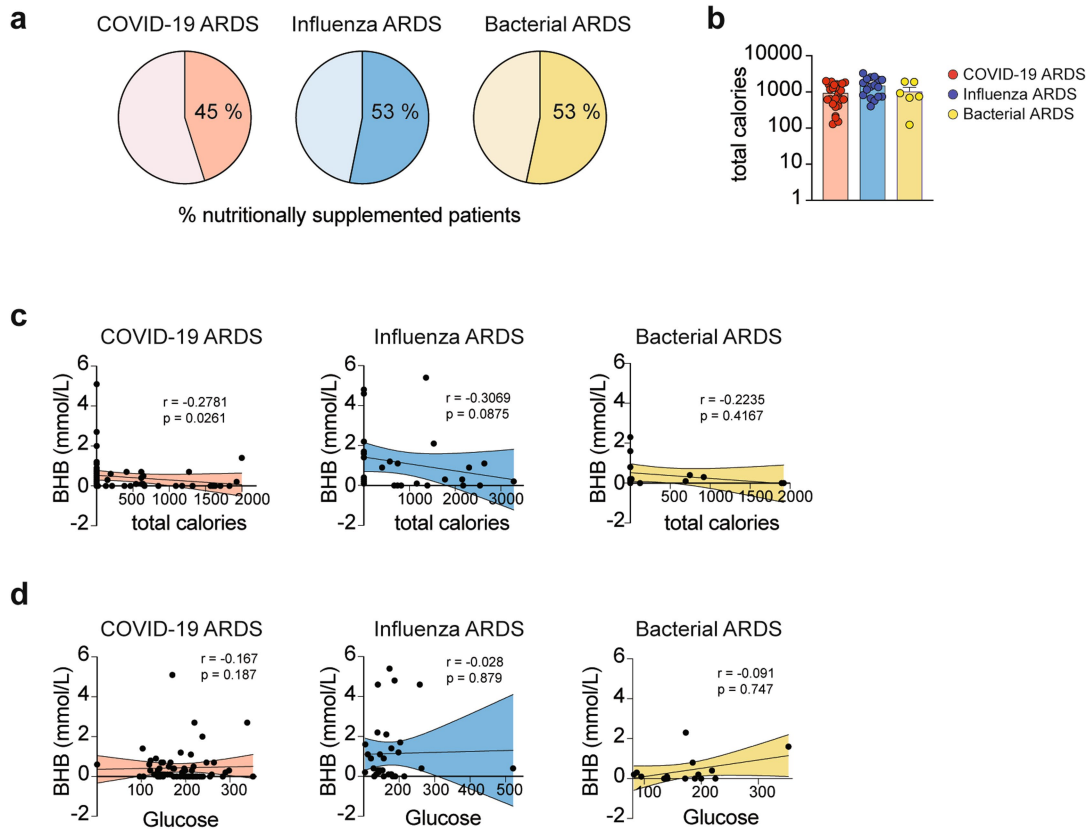
Peer review information *Nature* thanks Navdeep Chandel and the other, anonymous, reviewer(s) for their contribution to the peer review of this work. Peer reviewer reports are available.

Reprints and permissions information is available at <http://www.nature.com/reprints>.



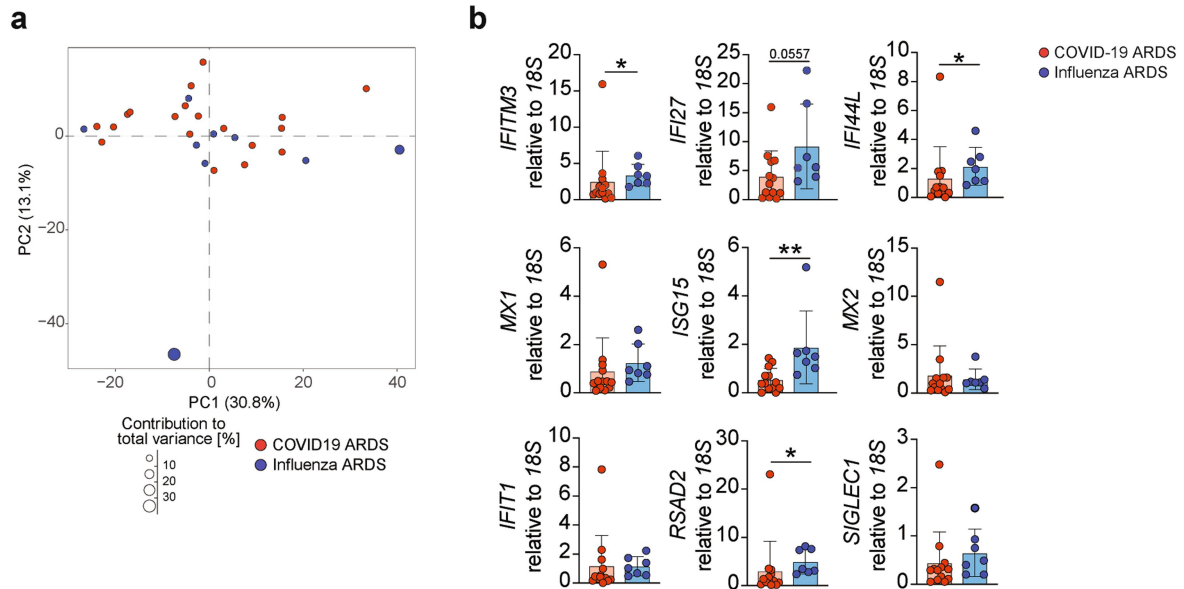
Extended Data Fig. 1 | Influenza A infection in mice induces ketogenesis. **a-c**, Mice were infected with IAV and euthanized on d 4, 7 and 10 for analysis. **(a)** Body weight and food uptake were monitored every day. **(b)** Heat maps depicting the quantification of BHB and glucose levels in plasma and lung. **(c)** Fold change of gene transcripts regulating ketogenesis in the liver

(*Hmgcs2*, *Cpt1a*). **(a-c)**, Data representative of three independent experiments with **(a)** $n = 4$ **(b, c)** $n = 6$ mice per experimental group. All graphs display mean \pm s.e.m. Statistics were assessed by **(d)** ordinary one-way ANOVA (Tukey's correction), not significant (not indicated) $p > 0.05$; ** $p < 0.01$.



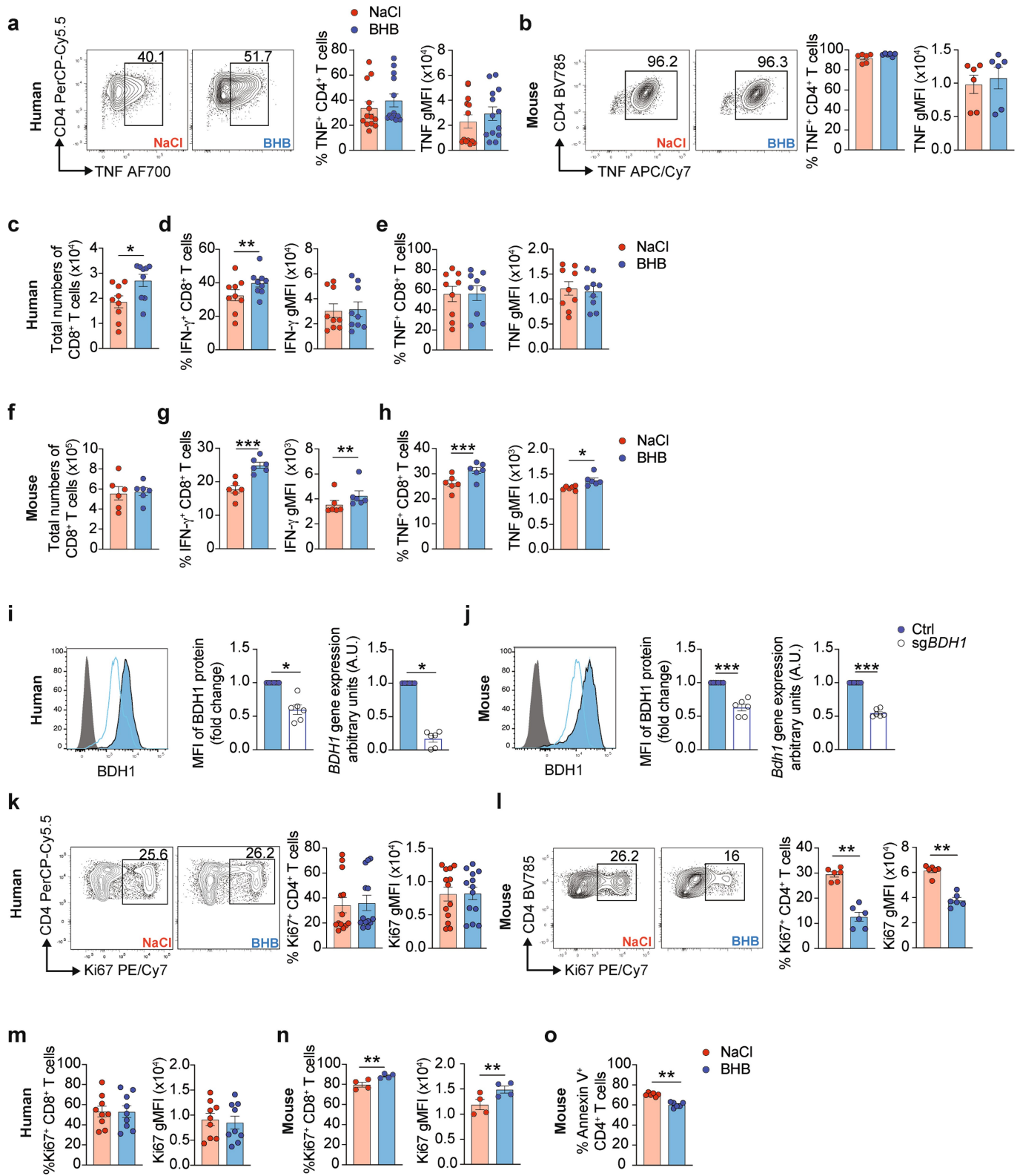
Extended Data Fig. 2 | Ketogenesis is not influenced by glucose or nutrient intake. **a**, Percentage of the nutritionally supplemented patients in the indicated groups. **b**, Quantification of total calories of nutritionally supplemented patients in the indicated groups (COVID-19 $n = 27$, Influenza $n = 17$ and bacterial $n = 6$). **c, d**, Plots correlating BHB levels and total calories

(c) and glucose concentration (d) in patients with COVID-19 $n = 63$, Influenza $n = 32$ or bacterial $n = 15$ ARDS. (b–d) Each dot represents a donor. (b) non-parametric one-way ANOVA (Kruskal–Wallis test), not significant (not indicated) $p > 0.05$. (c, d) the non-parametric Spearman correlation coefficient and the p values are indicated respectively as r and p in the plots.



Extended Data Fig. 3 | Interferon response in patients with severe respiratory viral infections. a, BALF RNA-seq from patients with severe COVID-19 ($n = 19$, red) and Influenza ($n = 9$, blue). PCA plot. **b**, Relative expression of interferon-stimulated genes (ISGs) in the BALF of patients with severe

COVID-19 ($n = 13$) and patients with influenza ($n = 7$). (**a, b**) Each dot represents a donor. Graphs display mean \pm s.d. Statistics were assessed by (**b**) two-tailed Student's t -test, not significant (not indicated) $p > 0.05$; * $p < 0.05$; ** $p < 0.01$.

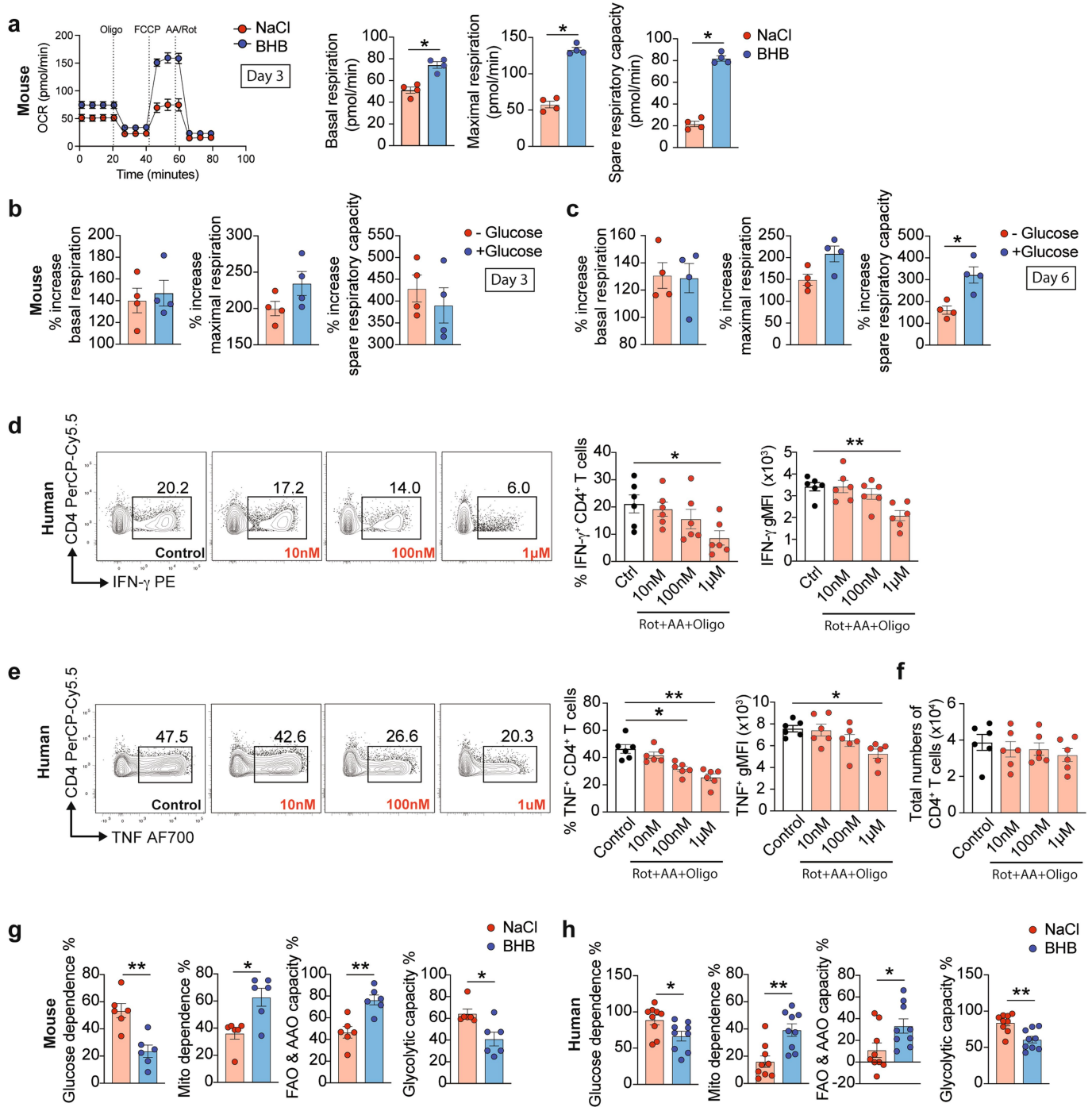


Extended Data Fig. 4 | See next page for caption.

Article

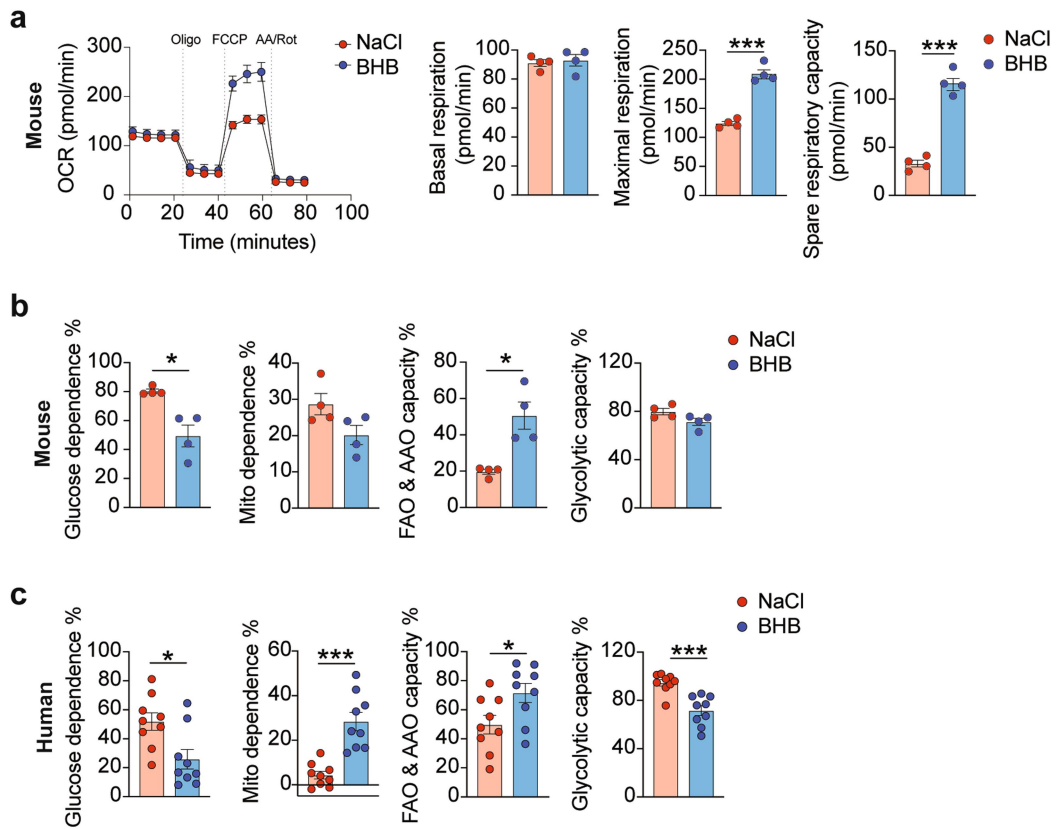
Extended Data Fig. 4 | BHB promotes T cell function in a BDH1-dependent manner. **a, c–e, k, m,** Human CD4⁺ T and CD8⁺ T cells were isolated from the blood of healthy donors and culture for 1 week in T_H1 polarizing conditions in the presence or absence of 5 mM BHB. **b, f–h, l, n, o,** Splenic mouse CD4⁺ and CD8⁺ T cells were activated in culture for 1 week in T_H1 polarizing conditions with or without 5 mM BHB. Representative flow plots and percentage of human (*n* = 13) **(a)** and mouse (*n* = 6) TNF⁺ CD4⁺ T cells and TNF gMFI **(b)**. Total numbers of live human CD8⁺ T cells **(c)**, percentage of IFN γ ⁺, IFN γ gMFI **(d)** and TNF⁺ CD8⁺ T cells, TNF gMFI **(e)** (*n* = 9) analysed by flow cytometry. Total number of live mouse CD8⁺ T cells **(f)** percentage of IFN γ ⁺ CD8⁺ T cells, IFN γ gMFI **(g)** and percentage of TNF⁺ CD8⁺ T cells, TNF gMFI **(h)** analysed by flow cytometry (*n* = 6). **(i, j)** Representative histograms and quantification of BDH1 protein by

flow cytometry (MFI) and gene expression analysis (fold change) of *BDH1* RNA in **(i)** human CD4⁺ T cells (*n* = 6) or **(j)** mouse naïve splenic CD4⁺ T cells (*n* = 6) mock treated or nucleofected with *Bdhl*-targeting (sg*Bdhl*) sgRNA/Cas9 RNPs cultured for 2 days in T_H1 polarizing conditions. Representative flow plots, percentages and gMFI of Ki-67 expression in human CD4⁺ T cells (*n* = 13) **(k)**, in mouse CD4⁺ T cells (*n* = 6) **(l)**, in human CD8⁺ T cells (*n* = 9) **(m)**, in mouse CD8⁺ T cells (*n* = 4) **(n)** and the % of mouse Annexin V⁺ CD4⁺ T cells (*n* = 6) **(o)** measured by flow cytometry. **(a, c–e, i–k, m)** Each dot represents a donor. **(b, f–h, l, n, o)** Data representative of three independent experiments with **(b, f–h, j, l, o)** *n* = 6 and **(n)** *n* = 4 mice in each experimental group. All graphs display mean \pm s.e.m. Statistics were assessed by **(a–o)** by two-tailed Student's *t*-test, not significant (not indicated) *p* > 0.05; **p* < 0.05; ***p* < 0.01; ****p* < 0.001.



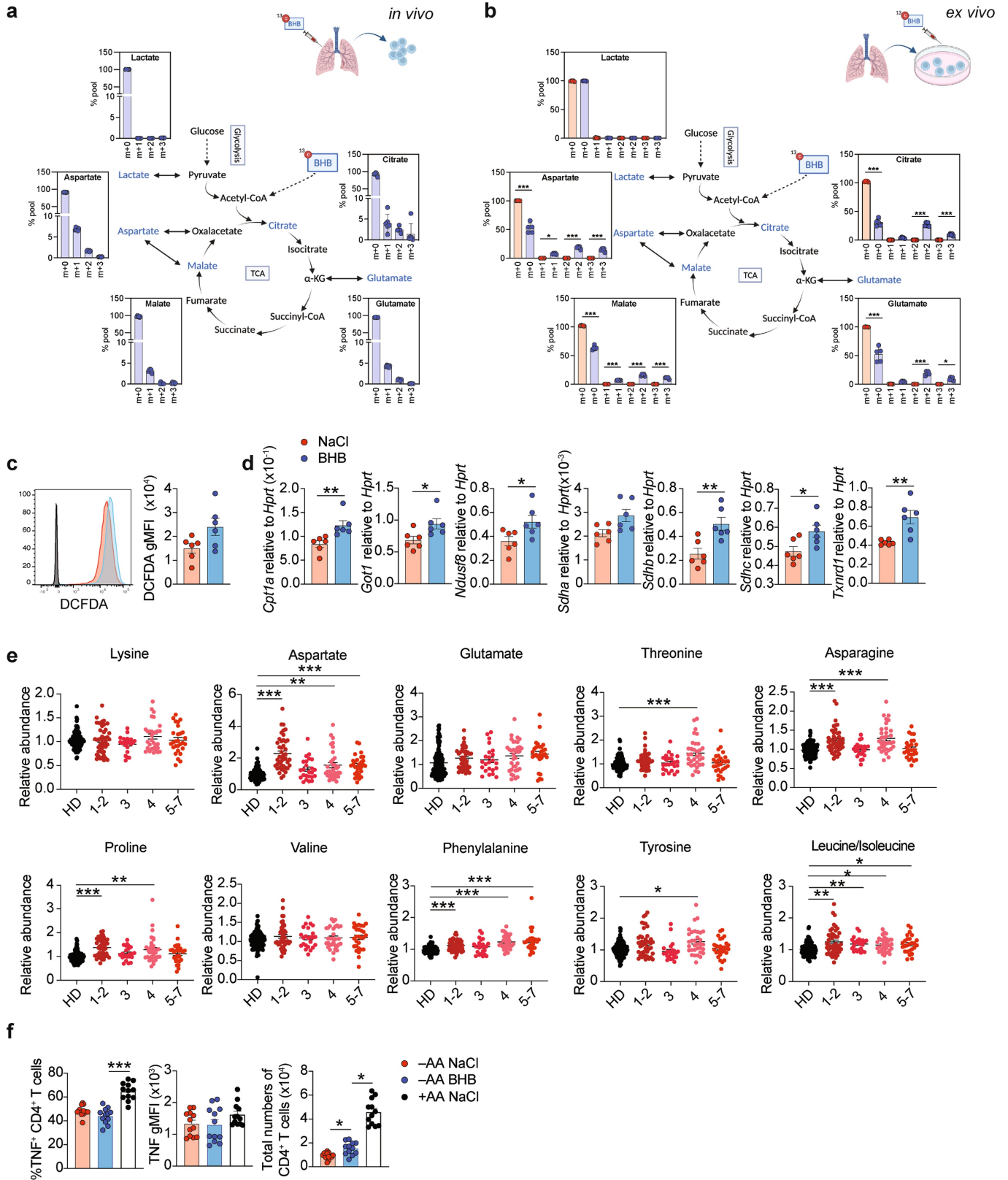
Extended Data Fig. 5 | BHB supports OXPHOS in T_H1 cells. **a-c**, Splenic mouse CD4⁺ T cells were activated in culture for 1 week (**a, c**) or 3 days (**b**) in T_H1 polarizing conditions with or without 5 mM BHB. Energy metabolism was monitored by extracellular flux analysis (**b, c**) in the presence or absence of glucose. Basal respiration, maximal respiration and spare respiratory capacity are depicted as the percentage of increase between NaCl and BHB treated cells ($n = 4$). **d-f**, Human CD4⁺ T cells were isolated from the blood of healthy donors ($n = 6$) and activated in culture for 2 days in T_H1 polarizing conditions, with or without OXPHOS inhibitors (rotenone, antimycin A and Oligomycin at the indicated concentrations). **(d-f)** Representative flow plots and **(d)** percentage

of IFN γ ⁺ CD4⁺ T cells and IFN γ gMFI. **(e)** TNF⁺ CD4⁺ T cells and TNF gMFI. **(f)** Total number of CD4⁺ T cells ($n = 6$). **g, h**, Splenic mouse CD4⁺ T cells ($n = 6$) and human CD4⁺ T cells isolated from the blood of healthy donors ($n = 9$) (**h**) were cultured for 1 week in T_H1 polarizing conditions with or without 5 mM BHB. Analysis of the energy metabolism by SCENITH ($n = 9$). **(d, e, f, h)** Each dot represents a donor. **(a-c, g)** Data representative of two independent experiments with **(a-c)** $n = 4$ or **(g)** $n = 6$ mice in each experimental group. All graphs display mean \pm s.e.m. Statistics were assessed by two-tailed Student's *t*-test and **(a-c, g-h)** non-parametric one-way ANOVA (Kruskal-Wallis test) **(d-f)**, not significant (not indicated) $p > 0.05$; * $p < 0.05$; *** $p < 0.01$.



Extended Data Fig. 6 | BHB supports mitochondrial fitness and OXPHOS in CD8⁺ T cells. **a, b**, Splenic mouse CD8⁺ T cells were activated in culture for 3 days in T_H1 polarizing conditions with or without 5 mM BHB. Energy metabolism was monitored by extracellular flux analysis (**a**) and by SCENITH (**b**) ($n = 4$). **c**, Human CD8⁺ T cells were isolated from the blood of healthy donors ($n = 9$) and activated in culture for 1 week in T_H1 polarizing conditions with or

without 5 mM BHB. Energy metabolism was monitored by SCENITH. (**c**) Each dot represents a donor. (**a, b**) Data representative of two independent experiments with $n = 4$ mice in each experimental group. All graphs display mean \pm s.e.m. (**a-c**) Statistics were assessed by two-tailed Student's *t*-test and, not significant (not indicated) $p > 0.05$; * $p < 0.05$; *** $p < 0.001$.

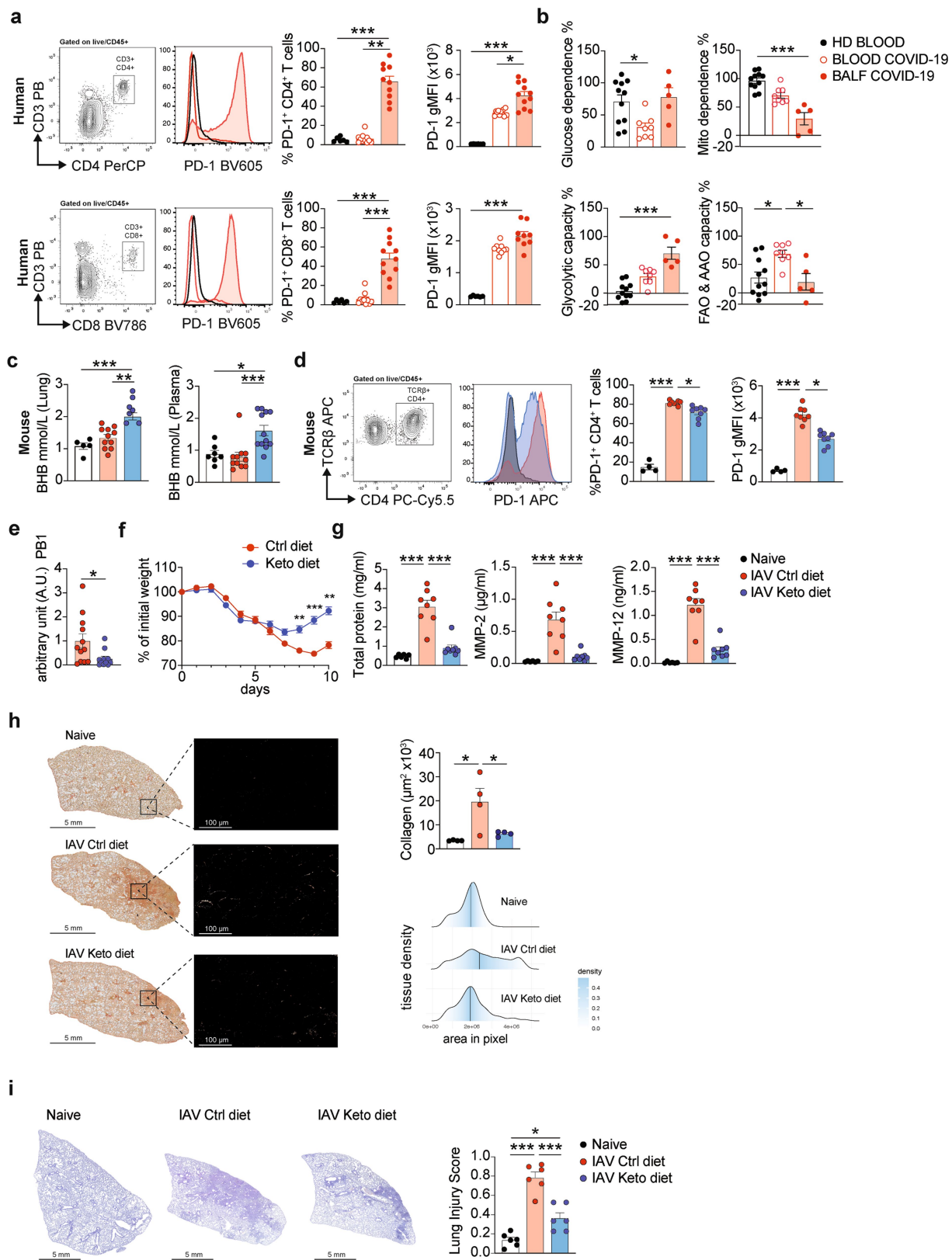


Extended Data Fig. 7 | See next page for caption.

Article

Extended Data Fig. 7 | BHB is a carbon source for CD4⁺ T cells in the infected lung. **a**, C57BL/6 mice were infected with IAV for 7 days. ¹³C-BHB was injected i.p. 20 min before euthanizing the mice. Lung CD4⁺ T cells were isolated and analysed by MS. **b**, C57BL/6 mice were infected with IAV for 7 days. Lung CD4⁺ T cells were isolated and cultured for 2 h with ¹³C-BHB followed by mass spectrometric analysis. **c**, Splenic mouse CD4⁺ T cells were cultured in T_H1 polarizing conditions with or without 5 mM BHB. Detection of cellular ROS (DCFDA gMFI) by FACS ($n = 6$). **d**, Relative expression of metabolic gatekeeper enzymes ($n = 6$). **e**, Relative abundance of indicated amino acid in serum of patients with COVID-19. Data extracted from published metabolomic dataset³⁶.

f, Human CD4⁺ T cells were isolated from the blood of healthy donors ($n = 12$) and cultured for 1 week in T_H1 polarizing conditions with or without 5 mM BHB. Percentage of TNF⁺ CD4⁺ T cells, TNF gMFI and total numbers of live cells analysed by flow cytometry. (**a-b**) Results are from ($n = 3$) pooled mice for each data point (**a**, $n = 6$; **b**, $n = 5$). Figure was created using BioRender.com. (**c, d**) Data representative of three independent experiments with $n = 6$ mice in each experimental group. (**e, f**) Each dot represents a donor. All graphs display mean \pm s.e.m. Statistics were assessed by (**b-d**) by two-tailed Student's *t*-test or (**e, f**) non-parametric one-way ANOVA (Kruskal-Wallis test), not significant (not indicated) $p > 0.05$; * $p < 0.05$; ** $p < 0.01$; *** $p < 0.001$.



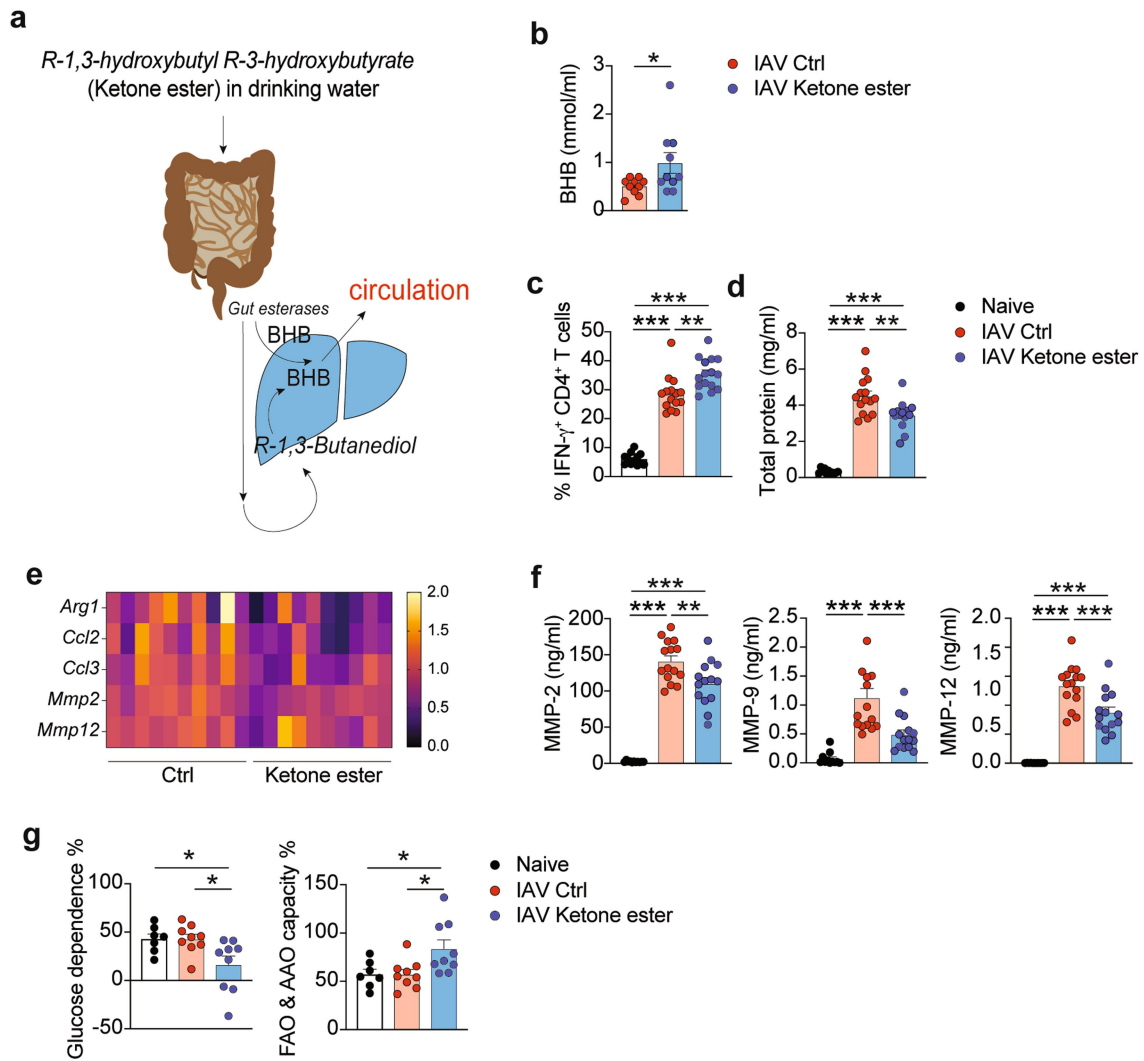
Extended Data Fig. 8 | See next page for caption.

Article

Extended Data Fig. 8 | A ketogenic diet promotes the resolution of

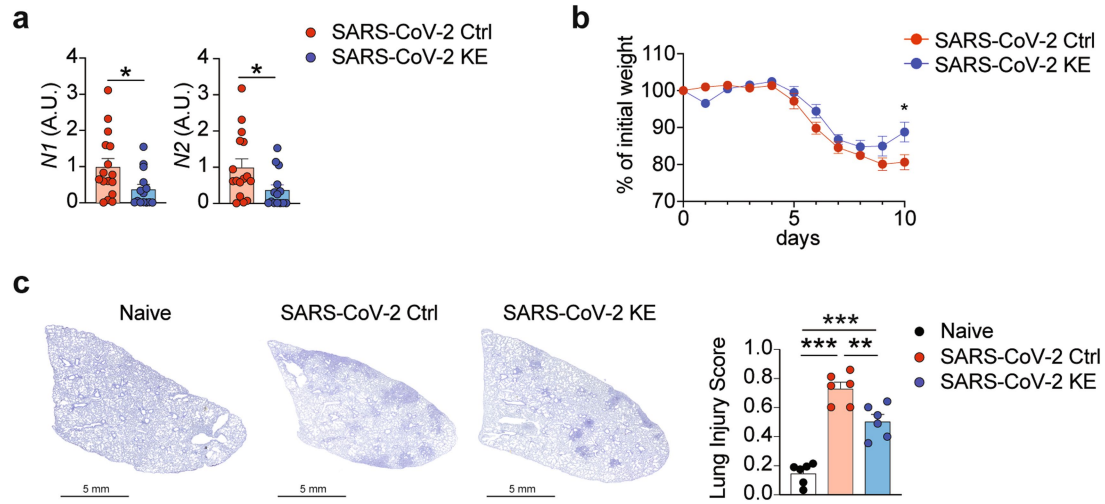
inflammation. a, b Analysis of CD4⁺ and CD8⁺ T cells in the blood of healthy donors (**a**, $n = 6$; **b**, $n = 11$, *black*) and the blood (**a**, $n = 11$; **b**, $n = 8$ *open red*) or BALF (**a**, $n = 11$; **b**, $n = 5$, *filled red*) of patients with severe COVID-19. (**a**) Gating strategy (left panel), representative histograms of PD-1 expression (right panel) and percentage of CD4⁺ and CD8⁺PD-1⁺ cells and gMFI of PD-1 ($n = 9$ *open red* and *filled red*) analysed by flow cytometry. (**b**) Metabolic characterization of CD8⁺ T cells by SCENITH. **c-h**. C57BL/6 mice were fed a control or ketogenic diet for 7 days followed by infection with IAV (d0). Mice were euthanized and analysed on d10. (**c**) Quantification of ketone bodies in the plasma and lung of mice (BHB lung: $n = 5$ naïve, $n = 11$ CD, $n = 7$ KD; BHB Plasma: $n = 7$ naïve, $n = 11$ CD, $n = 12$ KD). (**d**) Gating strategy (left panel), representative histograms of PD-1 expression (right panel) and percentage of CD4⁺PD-1⁺ cells and gMFI of PD-1 ($n = 4$ naïve, $n = 8$ CD and KD) (**e**) Relative expression of viral *PBI* RNA (viral load) on day 7

($n = 12$ CD and $n = 11$ KD). (**f**) Relative weight loss of infected mice ($n = 4$ CD and KD). (**g**) Quantification of total protein (BSA) and matrix metalloproteinases (MMPs) on day 14 ($n = 6$ naïve, $n = 8$ CD and KD). (**h**) Representative images stained with picosirius red of lungs and quantified for tissue density (shown as pixel count per image) and collagen deposition (total green area per image) ($n = 4$). (**i**) Representative image of lungs stained by haematoxylin and eosin (H&E) and lung injury score analysis ($n = 6$). Each dot represents a mouse. (**a-b**) Each dot represents a donor. (**c-g**) Pooled data from three independent experiments with $n = 4$ mice per experimental group. (**h, i**) Representative of three independent experiments with $n = 6$ in each experimental group. All graphs display mean \pm s.e.m. Statistics were assessed by (**a, b**) non-parametric one-way ANOVA (Kruskal–Wallis test), (**c, d, g-i**) ordinary one-way ANOVA (Tukey’s correction) and (**e, f**) two-tailed Student’s *t*-test, not significant (not indicated) $p > 0.05$; * $p < 0.05$; ** $p < 0.01$; *** $p < 0.001$.



Extended Data Fig. 9 | Treatment with ketone ester enhances T cell immunity and protects from IAV infection. **a**, Representation of ketone ester metabolism *in vivo*. **b-g**, C57BL/6 were challenged with IAV on day 0. Ketone ester were added in the drinking water for the duration of the whole experiment. Mice were euthanized on day 10. **(b)** Quantification of BHB in the blood ($n = 10$ for each experimental group). **(c)** Percentage of IFN γ ⁺ CD4⁺ T cells ($n = 12$ naïve, $n = 15$ Ctrl and $n = 15$ KE). **(d)** Total protein (BSA) measurements ($n = 11$ naïve, $n = 15$ Ctrl and $n = 14$ KE). **(e)** Heat map depicting the relative

expression of genes associated with fibrosis assessed by qRT-PCR ($n = 10$ for each experimental group). **(f)** Quantification of proteins associated with fibrosis in the lung ($n = 11$ naïve, $n = 15$ Ctrl and $n = 14$ KE). **(g)** Metabolic analysis of CD4⁺ T cells by SCENITH ($n = 7$ naïve, $n = 9$ Ctrl and KE). **(b-g)** Data pooled from three independent experiments with $n = 5$ mice per experimental group. All graphs display mean \pm s.e.m. Statistics were assessed by **(b)** two-tailed Student's *t*-test (**c, d, f, g**) ordinary one-way ANOVA (Tukey's correction), not significant (not indicated) $p > 0.05$; * $p < 0.05$; ** $p < 0.01$; *** $p < 0.001$.



Extended Data Fig. 10 | Treatment with ketone ester reduces pathology in SARS-CoV-2-infected mice. **a–c**, 8–12 weeks old male K18-hACE2 mice were infected with SARS-CoV-2. Mice were supplied with drinking water (Ctrl) or drinking water supplemented with ketone ester (KE) for the duration of the whole experiment. **(a)** Relative expression of viral *N1* and *N2* RNA quantified by qPCR on day 8 ($n = 16$ Ctrl and $n = 14$ KE) and **(b)** weight loss of infected mice ($n = 10$ Ctrl and

$n = 11$ KE). **(c)** Representative haematoxylin and eosin (H&E)-stained images of lungs and lung injury score analysis on day 12 post infection ($n = 6$). Data pooled from **(a)** four or **(b)** three or **(c)** two independent experiments. All graphs display mean \pm s.e.m. Statistics were assessed by **(a, b)** by two-tailed Student's *t*-test and **(c)** ordinary one-way ANOVA (Tukey's correction), not significant (not indicated) $p > 0.05$; * $p < 0.05$; ** $p < 0.01$; *** $p < 0.001$.

Extended Data Table 1 | Cohort summary

Characteristic	Healthy Donors (n=39)	Moderate COVID-19 (n=47)	COVID-19 ARDS (n=64)	Influenza ARDS (n=32)	Bacterial ARDS (n=15)	p
Age (y)	46 ± 16	64 ± 16.6	56 ± 12.3	54 ± 12.5	55 ± 18.2	0.0001
Male (%)	25 (64.1)	29 (63)	53 (82.8)	24 (75)	13 (86.7)	0.084
BMI	26.5 ± 5.9	27 ± 4.1	31.1 ± 6.1	31.2 ± 7	29.9 ± 6.3	0.0002
Diabetes (%)	N.A.	N.A.	20 (31.3)	6 (18.8%)	4 (26.7%)	0.45
Hyperlipidemia (%)	N.A.	N.A.	15 (23.4)	6 (18.8%)	4 (20%)	0.946
Arterial Hypertension (%)	N.A.	N.A.	42 (65.6)	15 (46.9%)	11 (73.3%)	0.13
Immunosuppression (%)	N.A.	N.A.	1 (1.6)	3 (9.4%)	3 (20%)	0.014
Steroid Exposure (%)	N.A.	N.A.	29 (45.3)	13 (40.6%)	5 (33.3%)	0.71
P/F Ratio	N.A.	N.A.	124.7 ± 70.1	108.3 ± 47.8	112.1 ± 63.4	0.8426
Death in ICU (%)	N.A.	N.A.	35 (54.7%)	13 (40.6%)	5 (33.3%)	0.23

Patient characteristics. Significant differences were calculated by Kruskal-Wallis or two-sided Fisher's exact test and expressed as mean ± s.d., 25% and 75% percentiles.

Reporting Summary

Nature Portfolio wishes to improve the reproducibility of the work that we publish. This form provides structure for consistency and transparency in reporting. For further information on Nature Portfolio policies, see our [Editorial Policies](#) and the [Editorial Policy Checklist](#).

Statistics

For all statistical analyses, confirm that the following items are present in the figure legend, table legend, main text, or Methods section.

n/a Confirmed

- The exact sample size (n) for each experimental group/condition, given as a discrete number and unit of measurement
- A statement on whether measurements were taken from distinct samples or whether the same sample was measured repeatedly
- The statistical test(s) used AND whether they are one- or two-sided
Only common tests should be described solely by name; describe more complex techniques in the Methods section.
- A description of all covariates tested
- A description of any assumptions or corrections, such as tests of normality and adjustment for multiple comparisons
- A full description of the statistical parameters including central tendency (e.g. means) or other basic estimates (e.g. regression coefficient) AND variation (e.g. standard deviation) or associated estimates of uncertainty (e.g. confidence intervals)
- For null hypothesis testing, the test statistic (e.g. F , t , r) with confidence intervals, effect sizes, degrees of freedom and P value noted
Give P values as exact values whenever suitable.
- For Bayesian analysis, information on the choice of priors and Markov chain Monte Carlo settings
- For hierarchical and complex designs, identification of the appropriate level for tests and full reporting of outcomes
- Estimates of effect sizes (e.g. Cohen's d , Pearson's r), indicating how they were calculated

Our web collection on [statistics for biologists](#) contains articles on many of the points above.

Software and code

Policy information about [availability of computer code](#)

Data collection

BD FACS Diva Software (version 6.1.3), Wave Desktop Software 2.6.1 (Seahorse - Agilent), Luminex xPONENT software (ThermoFisher Scientific): xPonent Version 4.2, QuantStudio Real-Time PCR software version 1.3 (ThermoFisher Scientific), ZEN 3.1 blue edition (ZEISS) Zen 3.1 blue edition (ZEISS): ZEN 3.1 Version: 3.1.0.0000

Data analysis

Qlucore (<https://www.qlucore.com/>)
 Prism 9 (<https://www.graphpad.com/>)
 FlowJo 10.7.2 (<https://www.flowjo.com/>)
 Legendplex Data Analysis Software (<https://legendplex.qognit.com/>)
 Milliplex analyst 5.1 flex: MILLIPLEX Analyst 5.1 Flex Version: 5.1.0.0 standard (<http://www.vigenetech.com/MILLIPLEXAnalystV51.htm>)
 Matlab software (The Mathworks, Natick, MA): Matlab Version: R2020b
 MetaboliteDetector (<https://md.tu-bs.de/>)
 RStudio (<https://www.rstudio.com/>)

For manuscripts utilizing custom algorithms or software that are central to the research but not yet described in published literature, software must be made available to editors and reviewers. We strongly encourage code deposition in a community repository (e.g. GitHub). See the Nature Portfolio [guidelines for submitting code & software](#) for further information.

Data

Policy information about [availability of data](#)

All manuscripts must include a [data availability statement](#). This statement should provide the following information, where applicable:

- Accession codes, unique identifiers, or web links for publicly available datasets
- A description of any restrictions on data availability
- For clinical datasets or third party data, please ensure that the statement adheres to our [policy](#)

All data generated or analysed in this study are included in this published article (as supplementary information files)

Field-specific reporting

Please select the one below that is the best fit for your research. If you are not sure, read the appropriate sections before making your selection.

- Life sciences Behavioural & social sciences Ecological, evolutionary & environmental sciences

For a reference copy of the document with all sections, see [nature.com/documents/nr-reporting-summary-flat.pdf](https://www.nature.com/documents/nr-reporting-summary-flat.pdf)

Life sciences study design

All studies must disclose on these points even when the disclosure is negative.

Sample size	Human Data: Sample size was based on donor availability. Mouse Data: No statistical method was used to determine sample size. The experimental groups were estimated based on previous experiment in the field (example of studies: Goldberg, E. L. et al. <i>Sci Immunol</i> , 2019; Ryu, S. et al. <i>Elife</i> 10, 2021)
Data exclusions	No data were excluded from this study
Replication	RNA seq analysis has been performed once, using the available donors from the described cohorts. Metabolic tracing analysis was conducted in vitro, in vivo and ex vivo. In vitro metabolic tracing analysis was performed once, pooling more than 5 mice per condition and analyzing at least 4 biological replicates. In vivo and ex vivo metabolic tracing analysis was performed twice, pooling more than 5 mice per condition and analyzing at least 3 biological replicates. All the other experiments have been repeated at least two times. Crucial experiments were validated independently by the authors of the manuscript with different technologies.
Randomization	Allocation was random for each experiment. Donors were assigned a number and shuffled at the beginning of the experiments. Co-housed wild type mice were randomly assigned to the control and keto diet groups or to the control and ketone ester groups.
Blinding	Cytokines measurement and histology was done in a single blinded fashion. Other experiments were not done in a blind fashion as the investigators need to design, conduct and analyze the data, thus they need to know the identification of the samples. Moreover, there were no subjective measurements.

Reporting for specific materials, systems and methods

We require information from authors about some types of materials, experimental systems and methods used in many studies. Here, indicate whether each material, system or method listed is relevant to your study. If you are not sure if a list item applies to your research, read the appropriate section before selecting a response.

Materials & experimental systems

n/a	Involved in the study
<input type="checkbox"/>	<input checked="" type="checkbox"/> Antibodies
<input checked="" type="checkbox"/>	<input type="checkbox"/> Eukaryotic cell lines
<input checked="" type="checkbox"/>	<input type="checkbox"/> Palaeontology and archaeology
<input type="checkbox"/>	<input checked="" type="checkbox"/> Animals and other organisms
<input type="checkbox"/>	<input checked="" type="checkbox"/> Human research participants
<input type="checkbox"/>	<input checked="" type="checkbox"/> Clinical data
<input checked="" type="checkbox"/>	<input type="checkbox"/> Dual use research of concern

Methods

n/a	Involved in the study
<input checked="" type="checkbox"/>	<input type="checkbox"/> ChIP-seq
<input type="checkbox"/>	<input checked="" type="checkbox"/> Flow cytometry
<input checked="" type="checkbox"/>	<input type="checkbox"/> MRI-based neuroimaging

Antibodies

Antibodies used	Human antibodies: CD4 (Biolegend, RPA-T4, cat#: 300530, lot#: B313463), CD8a (Biolegend, SK1, cat#: 344740, lot#: B317062), CD45 (Biolegend, HI30, cat#: 304024, lot#: B306873), CD279 (PD-1) (Biolegend, EH12.2H7, cat#: 329905, lot#: B312088), TNF- α (Biolegend, MAb11, cat#: 502928, lot#: B337546), Ki67 (Biolegend, Ki-67, cat#: 350525, lot#: B269861), IFN γ (Biolegend, 4S.B3, cat#: 502509, lot#: B336564), CD4 biotin (Biolegend, RPA-T4, cat#: 300504, lot#: B307100), CD8 biotin (Biolegend, RPA-T8, cat#: 301004, lot#:
-----------------	--

B323949), anti-puromycin (EMD Millipore, 12D10, cat#: MABE343-AF488, lot#: 3605504), anti-BDH1 (abcam, ,cat#: ab193156, lot#:GR3397506-8). Human TruStain FcXTM (Fc Receptor Blocking Solution, cat# 422302)

Mouse antibodies: CD45 (Biolegend, 30-F11, cat#: 103154, lot#: B330012), CD4 (Biolegend, RM4-5, cat#: 100552, lot#: B311987), CD8a (BD biosciences, 53-6.7, cat#: 100712, lot#: 6152735), TCRb (Biolegend, H57-597, cat#: 109228, lot#: B332502), CD279 (PD-1) (Biolegend, 29F.1A12, cat#: 135229, lot#: B333067), Ki67 (Biolegend, 16A8, cat#: 652426, lot#: B264069), IFNg (Biolegend, XMG1.2, cat#: 505806, lot#: B240651), TNF-a (Biolegend, MP6-XT22, cat#: 506344, lot#: B311548), anti-puromycin (EMD Millipore, 12D10, cat#: MABE343-AF488, lot#: 3605504), anti-BDH1 (abcam, ,cat#: ab193156, lot#:GR3397506-8)

Validation

Antibodies were all validated by suppliers.

Animals and other organisms

Policy information about [studies involving animals](#); [ARRIVE guidelines](#) recommended for reporting animal research

Laboratory animals

Mice were housed at a density of maximum 5 animals per cage, on a 12h light-dark cycle. Both female and male mice between 6-14 weeks were analyzed in this study. C57BL/6N and K18-hACE2 mice were included in this study.

Wild animals

Wild animals were not used for this study.

Field-collected samples

This study does not include samples collected from the field.

Ethics oversight

Animal care was in accordance with the local and regional ethics committees guidelines for animal experiments.

Note that full information on the approval of the study protocol must also be provided in the manuscript.

Human research participants

Policy information about [studies involving human research participants](#)

Population characteristics

A total of 196 individuals (157 patients and 39 healthy donors) were included in this study. The cohort was composed of patients with viral or bacterial ARDS (Influenza n=32; COVID-19 n=64; Bacterial n=15) or moderate COVID-19 (n=46) hospitalized in the following hospitals: University Hospital Bonn, Hannover Medical School, Radboud University Medical Center Nijmegen and University Hospital Essen. ARDS patients were diagnosed according to the Berlin Definition, moderate COVID-19 patients were hospitalized due to lower respiratory disease without need for critical care or ventilation support. Healthy Donors were randomly selected (age, sex).
Ethic committee approval of license numbers: 313/15 and 008/16

Recruitment

Patients were identified through screening of EMR records for potential enrollment with no self selection. Serum samples from patients with moderate COVID-19 or ARDS due to Influenza, COVID-19 or bacterial pneumonia were obtained from University Hospital Bonn, Radboud University Medical Center Nijmegen, University Hospital Essen and Hannover Medical School. Healthy donors and BALF samples were obtained from the University Hospital Bonn. Patients with moderate COVID-19 were hospitalized but not requiring intensive care. ARDS was defined according to the Berlin Definition. Informed consent was obtained by trained staff and sample collection commenced within the first 24h after hospital admission.

Ethics oversight

All human samples were obtained with approval by the local institutional research ethics boards of the University Hospital Bonn (313/15, 088/16, 468/20), Medical Chamber North Rhine (2020157), University Hospital Essen (20-9216 BO), Hannover Medical School (8146_BO_K_2018) and the CMO regio Arnhem-Nijmegen (Radboud) (CMO 2020 6344 and CMO 2016 2963).

Note that full information on the approval of the study protocol must also be provided in the manuscript.

Clinical data

Policy information about [clinical studies](#)

All manuscripts should comply with the ICMJE [guidelines for publication of clinical research](#) and a completed [CONSORT checklist](#) must be included with all submissions.

Clinical trial registration

N/A

Study protocol

N/A

Data collection

N/A

Outcomes

N/A

Plots

Confirm that:

- The axis labels state the marker and fluorochrome used (e.g. CD4-FITC).
- The axis scales are clearly visible. Include numbers along axes only for bottom left plot of group (a 'group' is an analysis of identical markers).
- All plots are contour plots with outliers or pseudocolor plots.
- A numerical value for number of cells or percentage (with statistics) is provided.

Methodology

Sample preparation

Isolation of peripheral blood mononuclear cells (PBMC) and single cell suspension was achieved by Ficoll® Paque Plus (Millipore Sigma) density gradient centrifugation. Serum was collected from each patient and donor and used for RNA isolation and cytokine quantification. Prior to FACS analysis, BALF samples were collected, washed and fixed with 4% Paraformaldehyde (PFA), while red blood cells lysis with Ammonium-Chloride-Potassium (ACK) lysing buffer was performed for blood samples accordingly to manufacturer's instructions.

Mouse lung tissues were diced and digested with 0.25 mg/ml Liberase TL (Roche) and 1 mg/ml DNase I (Sigma) at 37°C for 1 h. Isolated lung cells were further purified using a 37.5% Percoll gradient, followed by lysis of red blood cells with Ammonium-Chloride-Potassium (ACK) lysing buffer.

Cells were stained with surface antibodies and Fixable Viability Dye (Zombie UV - Biolegend) in PBS 2% FCS (FACS buffer) for 30 minutes at 4°C in the presence of Human (Biolegend) or mouse Fc block (BioXcell). For experiments involving intracellular staining of cytokines, cells were stimulated for 6 hours with Phorbol 12-myristate 13-acetate (50 ng/ml) (PMA; Peprotech I) and ionomycin (1 µg/ml) (Peprotech) in the presence of brefeldin A (1 µg/ml) (GolgiPlug, BD Biosciences). Cells were washed with FACS buffer followed by fixation with Foxp3 fixation/permeabilization kit (eBioscience) in accordance with the manufacturer's instructions, and stained with intracellular antibodies for 60 minutes at 4°C.

Instrument

LSRFortessa (BD Biosciences)

Software

BD FACS Diva Software (version 6.1.3)
FlowJo 10.7.2 (<https://www.flowjo.com/>)
Prism 9 (<https://www.graphpad.com/>)

Cell population abundance

Cell were not sorted by FACS. Human CD4+ and CD8+ T cells were purified from PBMC using magnetic positive selection with biotin human anti-CD4+ or anti-CD8+ antibodies followed by incubation with Streptavidin-coupled magnetic microbeads (Biolegend) and positive selection with magnets. Mouse Naïve CD4+ T and CD8+ T cells cells were purified from mouse spleens using the magnetic negative selection kit (Mojosort mouse CD4 naïve T cell isolation kit, Biolegend; CD8+ T cell isolation kit, Miltenyi) according to manufacturer's instructions. Purity was above 90% and was checked by FACS.

Gating strategy

Human CD4 gating strategy: live CD45+ CD3+ CD8- CD4+
Human CD8 gating strategy: live CD45+ CD3+ CD4- CD8+

Mouse CD4 gating strategy: live CD45+ TCR+ CD8- CD4+
Mouse CD4 gating strategy: live CD45+ TCR+ CD4- CD8-

- Tick this box to confirm that a figure exemplifying the gating strategy is provided in the Supplementary Information.